

PAPER

# Global linear stability analysis of kinetic trapped ion mode (TIM) in tokamak plasma using the spectral method

To cite this article: D Mandal *et al* 2023 *Plasma Phys. Control. Fusion* **65** 055001

View the [article online](#) for updates and enhancements.

## You may also like

- [Hamiltonian dynamics of preferential attachment](#)  
Konstantin Zuev, Fragkiskos Papadopoulos and Dmitri Krioukov
- [Impurity pinch generated by trapped particle driven turbulence](#)  
K Lim, E Gravier, M Lesur *et al.*
- [Impact of energetic particle orbits on long range frequency chirping of BGK modes](#)  
H. Hezaveh, Z.S. Qu, B. Layden *et al.*

# Global linear stability analysis of kinetic trapped ion mode (TIM) in tokamak plasma using the spectral method

D Mandal<sup>1,\*</sup> , M Lesur<sup>1</sup> , E Gravier<sup>1</sup> , J N Sama<sup>1</sup> , A Guillevic<sup>1</sup> , Y Sarazin<sup>2</sup>   
and X Garbet<sup>2</sup> 

<sup>1</sup> Université de Lorraine, CNRS, IJL, Nancy, F-54000, France

<sup>2</sup> CEA, IRFM, Saint-Paul-Lez-Durance, F-13108, France

E-mail: [debraj.mandal@univ-lorraine.fr](mailto:debraj.mandal@univ-lorraine.fr)

Received 21 November 2022, revised 31 January 2023

Accepted for publication 23 February 2023

Published 15 March 2023



CrossMark

## Abstract

Trapped ion modes (TIMs) belong to the family of ion temperature gradient (ITG) modes, which are one of the important ingredients in heat turbulent transport at the ion scale in tokamak plasmas. A global linear analysis of a reduced gyro-bounce kinetic model for trapped particle modes is performed, and a spectral method is proposed to solve the dispersion relation. Importantly, the radial profile of the particle drift velocity is taken into account in the linear analysis by considering the magnetic flux  $\psi$  dependency of the equilibrium Hamiltonian  $H_{\text{eq}}(\psi)$  in both the quasi-neutrality equation and equilibrium gyro-bounce averaged distribution function  $F_{\text{eq}}$ . Using this spectral method, linear growth rates of TIM instability in the presence of different temperature profiles and precession frequencies of trapped ions, with an approximated constant Hamiltonian and the exact  $\psi$  dependent equilibrium Hamiltonian, are investigated. The growth rate depends on the logarithmic gradient of temperature  $\kappa_T$ , density  $\kappa_n$  and equilibrium Hamiltonian  $\kappa_\Lambda$ . With the exact  $\psi$  dependent Hamiltonian, the growth rates and potential profiles are modified significantly, compared to the cases with an approximated constant Hamiltonian. All the results from the global linear analysis agree with a semi-Lagrangian based linear Vlasov solver with good accuracy. This spectral method is very fast and requires much less computation resources compared to a linear version of the Vlasov-solver based on a semi-Lagrangian scheme.

Keywords: linear stability analysis, electrostatic turbulence, spectral method, gyrokinetic theory and simulation, turbulence in tokamak, trapped ion mode instability, drift wave turbulence

(Some figures may appear in colour only in the online journal)

## 1. Introduction

Low frequency and low wavenumber turbulence, which is mainly generated by the ion temperature gradient (ITG) [1–3] and trapped electron mode (TEM) [4, 5] instabilities, plays a dominant role in the anomalous radial energy and particle

transport in magnetically confined fusion plasmas. The ITG is an important ingredient in anomalous ion heat transport in the tokamak, whereas TEM turbulence drives electron particles and heat transport. ITG-driven modes are frequently observed and relevant in tokamak plasma experiments [6, 7]. The trapped ion mode (TIM) belongs to this family of ITG modes, and is driven by the resonant motion of trapped ions [8]. The trapped ion instability is characterized by frequencies of the order of the trapped ion precession frequency and

\* Author to whom any correspondence should be addressed.

radial scales of the order of several banana widths. Although TIMs have lower frequency and a longer wavelength compared to TEMs, the TIM has similar physical mechanisms to the TEM in the linear regime. Both the TIM and TEM are driven by precession frequencies of ions and electrons respectively, and are generated in the presence of ion and electron equilibrium gradients respectively [9, 10]. However, in the nonlinear regime, they depart from each other due to different responses of zonal flows [11–13]. It is essential to properly estimate the linear growth rate of these trapped-particle instabilities to understand their influence on nonlinear saturation, the turbulent nature of the system, and the associated transport. Although the TEM is more directly relevant to tokamak turbulence and transport, the TIM in numerical simulation is much more tractable and shares essential similarities with the TEM in the linear phase. Therefore, here we focus on the TIM instability.

During last few decades, ion turbulence in magnetically confined plasmas has been intensively studied in fluid simulations [14–16], the fluid-kinetic hybrid electron model for studying low frequency electro-magnetic turbulence [17], particle-in-cell based gyrokinetic simulations [18–20], continuum Vlasov approach gyrokinetic simulations in the Eulerian grid [21],  $\delta f$ -particle-in-cell based simulations for bounce-averaged kinetic equations obtained by phase-space Lagrangian Lie-perturbation theory [22, 23], and semi-Lagrangian based reduced bounce averaged gyrokinetic simulations [8, 9, 24]. However, a kinetic model is necessary to capture the kinetic features of TIMs, and a full five-dimension (5D) gyrokinetic model demands more computer resources. We consider a reduced four-dimension (4D) gyro-kinetic model with averaging over gyro-motion and the banana-orbit motion, and the adiabatic response of passing particles [8]. This allows us to study the TIM instability, driven through the resonant interactions of trapped ions with a wave, separately from the ITG instability, which is generated in the presence of an ion pressure gradient.

The TIM instability is driven by the ITG  $\nabla_{\perp} T_i$  and  $\nabla B$  drift. In the unfavorable curvature region of a tokamak, the temperature gradient is aligned with the magnetic field gradient; particles in the lower temperature region drift more slowly than in the higher temperature region, which yields a charge separation in the presence of a perturbed density profile. The electric field generated by this charge separation creates an  $E \times B$  drift motion, which enhances the initial perturbation, hence leading to an instability. Although the nonlinear evolution of this TIM instability is interesting in the context of turbulent transport, it is first worth studying the linear properties of this instability. A local-linear analysis of TIM instability using this reduced gyro-kinetic model was reported by Drouot *et al* [9], where the values of all relevant parameters were considered at a particular radial location. The linear version of the simulation code TERESA [8, 25, 26], which is based on a semi-Lagrangian method, is able to solve the modeled equations in the linear limit with radial profiles of all relevant parameters [27]. Here, we present an alternative *global-linear analysis* by solving the modeled equations of

this reduced gyro-kinetic model in the linear limit using a spectral method [28, 29], which takes into account the radial profiles of all relevant parameters, while saving a lot of computational resources compared to the linear version of the TERESA code.

Moreover, until now, the TIM instability, and its growth rate in the presence of different temperature profiles and variations in precession frequency have been studied with the assumptions that the temperature profile varies linearly with  $\psi$  and that the precession frequency remains constant throughout the simulation box, which is a good approximation for a simulation region, situated sufficiently far from the edge (i.e. the last closed flux surface (LCFS) in our model) and the core region of a tokamak. Here, using this solver, based on a spectral method, we have studied the effects on the TIM instability of different temperature profiles  $T_i(\psi)$ , and precession frequency profiles  $\Omega_D(\psi, \kappa)$  as a function of the magnetic flux surface  $\psi$  and trapping parameter  $\kappa$ , which is associated with the *pitch angle* variation of trapped particles. All the temperature and precession frequency profiles are relevant to different experimental observations. Depending on the temperature profiles and precession frequency values, we found different growth rates of the TIM instability and different potential solutions of the system, which are significantly different from the previous local linear analysis results [9]. Additionally, for incorporating the variation of particles drift velocity with magnetic flux  $\psi$ , we have modified the previous gyro-bounce averaged kinetic model by introducing the  $\psi$  dependency of the equilibrium Hamiltonian  $H_{\text{eq}}$  in the quasi-neutrality equation and the equilibrium distribution function, which was neglected in the previous model where the equilibrium Hamiltonian was approximated by the energy  $E$  of the particles:  $H_{\text{eq}} \approx E$  [25]. This new modification changes the growth-rate profile of TIM instability, and changes the potential solution of the system. The growth rate depends on the logarithmic gradients of temperature, density and equilibrium Hamiltonian, respectively  $\kappa_T$ ,  $\kappa_n$  and  $\kappa_{\Lambda}$ . All the results from this spectral method are successfully compared with the new linear version of TERESA, which incorporates the  $\psi$  and  $\kappa$  dependency of precession frequency. Therefore, this newly proposed method for global linear analysis of TIM instability, and the associated results help us to understand the threshold/beginning of turbulent transport in the tokamak by TIMs, and also explain possible dominant modes of this instability in a nonlinear regime.

Our paper is organized as follows. Section 2 presents the bounce-averaged gyrokinetic model, where a brief description of the previous nonlinear model, along with crucial upgrades, are discussed. The formulation of global linear analysis of this nonlinear model is also presented in this section. Section 3 presents a numerical solver based on the spectral method for solving the dispersion relation, which is derived from global linear analysis. The effect of different temperature profiles and precession frequency profiles on the TIM instability in the limit  $H_{\text{eq}} \approx E$  is discussed in section 4. In section 5, the effect of the inverse gradient length of equilibrium Hamiltonian  $\kappa_{\Lambda}$ , on the TIM instability is presented. Section 6 presents the conclusions.

## 2. The bounce-averaged gyrokinetic model and its modifications due to exact Hamiltonian $H(\psi, \kappa)$

An electrostatic reduced collisionless bounce-averaged gyrokinetic model was developed by Depret, Sarazin and Darnet [8, 9, 25, 26]. We adopt this model to study the stability of TIMs. In this model, the system evolves on a timescale of the order of the trapped particle precession frequency  $\omega_D$ , which allows filtering out the large frequencies  $\omega_c$  (cyclotron frequency) and  $\omega_b$  (bounce frequency around banana orbit) ( $\omega_D \ll \omega_b \ll \omega_c$ ), and simplifies the effect of length scales  $\rho_c$  (gyro-radius) and  $\delta_b$  (banana width). The dynamics of the gyro and bounce averaged trapped particles or *banana center* distribution function  $f_s$  is determined by the kinetic Vlasov equation,

$$\frac{\partial f_s}{\partial t} - [J_{0,s}\phi, f_s]_{\alpha, \psi} + \frac{\Omega_D(\psi, \kappa)E}{Z_s} \frac{\partial f_s}{\partial \alpha} = 0 \quad (1)$$

where  $\phi$  is the electrostatic potential.  $Z_s$  is the charge number of the species.  $[\cdot \cdot]_{\alpha, \psi}$  is the Poisson bracket in the phase space of toroidal precession angle  $\alpha$  and poloidal magnetic flux  $\psi$  ( $\psi \sim -r^2$ , is used as a radial co-ordinate, where  $r$  is the radius of the tokamak). The magnetic flux-function is calculated from the integration  $\psi(r) \sim -B_{\min} \int_0^r \frac{r}{q_0} dr$ , where the negative sign stems from the convention that the direction of poloidal magnetic field  $B_\theta$  and the normal direction of the internal poloidal surface element are opposite to each other. Then,  $\psi$  is shifted and normalized such that  $\hat{\psi}$  is always positive, and  $\hat{\psi} \in [0, 1]$  corresponds to a limited radial extent of the tokamak with  $\hat{\psi} = 0$  being associated with the edge, toward the LCFS, and  $\hat{\psi} = 1$  being associated with the core, toward the hottest central region of the tokamak. This model is not valid inside the open field line regions, where most of the trajectories intercept plasma-facing components. The normalization of  $\psi$  and other essential physical quantities are given in table 1, where dimensionless normalized quantities are noted with hat. However, in the main text, the hat notation is omitted for clarity.  $E\Omega_D/Z_s = \omega_{d,s}$  is the energy dependent precession frequency of species  $s$ ,

$$\omega_{d,s} = \frac{q(r)}{r} \frac{E}{q_s B_{\min} R_0} \bar{\omega}_d, \quad (2)$$

where  $q$ , and  $R_0$  are the safety factor, and major radius of the tokamak, respectively.  $q_s$  is the electric charge of the species  $s$ ,  $B_{\min}$  is the minimal strength of the magnetic field on a field line,  $E \equiv \frac{1}{2} m_s v_{G\parallel}^2 + \mu B_G$  is the particle kinetic energy,  $\mu \equiv \frac{m_s v_\perp^2}{2B_G}$  is the magnetic moment, where subscript  $G$  refers to the quantities computed at the position of the guiding center, and

$$\bar{\omega}_d = \frac{2\mathcal{E}(\kappa^2)}{\mathcal{K}(\kappa^2)} - 1 + 4s_0(r) \left( \frac{\mathcal{E}(\kappa^2)}{\mathcal{K}(\kappa^2)} + \kappa^2 - 1 \right), \quad (3)$$

where  $\kappa = \sqrt{\frac{1-\lambda}{2\varepsilon\lambda}}$  is the trapping parameter which can vary between 0 (for deeply trapped particles) to 1 (at separatrix for a barely trapped particle).  $\varepsilon = a/R_0$  is the inverse of the aspect

**Table 1.** Normalization of the plasma parameters. Physical quantities are noted without a hat, and dimensionless quantities are noted with a hat. Here  $\omega_{d,0} = q_0 T_0 / (e r_0 R_0 B_0)$  is a typical precession frequency of a strongly trapped ion at  $E = T_0$ .  $n_0$  and  $T_0$  are arbitrary normalizing ion density and temperature such that  $\hat{n}_s = \hat{T} = 1$  at  $\hat{\psi} = 0$ . The quantity  $L_\psi$  is the radial size of the simulation box in the magnetic flux unit. The minor radius  $a$ , the Larmor radius  $\rho_{c,0}$ , and the banana width  $\delta_b$  are all expressed in units of  $\psi$ . However, in the main text, the hat notation is omitted for clarity.

Quantity	e.g.	Normalization
Time	$t, \omega^{-1}$	$\hat{t} = \omega_{d,0} t$
Poloidal magnetic flux	$\psi, a, \rho_{c,0}, \delta_b$	$\hat{\psi}(r) = \frac{\psi(r) - \psi(a)}{L_\psi}$
Electric potential	$\phi$	$\hat{\phi} = \phi / (\omega_{d,0} L_\psi)$
Energy	$E$	$\hat{E} = E / T_0$
Density	$n_s$	$\hat{n}_s = n_s / n_0$
Temperature	$T$	$\hat{T} = T / T_0$
Distribution function	$f_s, F_{\text{eq}}$	$\hat{f}_s = \frac{1}{n_0} \left( \frac{2\pi T_0}{m} \right)^{3/2} f_s$

ratio of the tokamak,  $a$  is the minor radius of the tokamak, and for a tokamak with a large aspect ratio, usually, the quantity  $\varepsilon < 1$ .  $\lambda = \mu B_{\min}(\psi) / E$  is the pitch angle,  $s_0 = \frac{r}{q(r)} \frac{dq}{dr}$  is the magnetic shear, and  $\mathcal{K}(\kappa^2)$  and  $\mathcal{E}(\kappa^2)$  are the complete elliptic functions of the first and second kind, respectively. The operator  $J_{0,s}$  performs two successive averages: the gyro-average and the bounce-average, which are the average over the cyclotron motion and the banana motion, respectively for the species  $s$ —these are (according to the ‘Padé’ expression [25]).

$$J_{0,s} = \left( 1 - \frac{E}{T_{\text{eq},s}(0)} \frac{\delta_{b0,s}^2}{4} \partial_\psi^2 \right)^{-1} \left( 1 - \frac{E}{T_{\text{eq},s}(0)} \frac{q^2 \rho_{c0,s}^2}{4L_\psi^2} \partial_\alpha^2 \right)^{-1}, \quad (4)$$

where  $\rho_{c0,s} = \frac{m_s v_\perp}{q_s B}$  and  $\delta_{b0,s} = q \rho_{c0,s} / \sqrt{\varepsilon}$  are the Larmor radius and the banana width (in unit of  $\psi$ ) computed at temperature  $T_0$ .  $T_{\text{eq},s}(0)$  is the equilibrium temperature of species  $s$  at  $\psi = 0$ .

Self-consistency is ensured by a quasi-neutrality constraint, including a polarization term  $\bar{\Delta}_s \phi$ , where  $\bar{\Delta}$  is a non-isotropic Laplacian operator,

$$\bar{\Delta}_s = \left( \frac{q \rho_{c0,s}}{L_\psi} \right)^2 \frac{\partial^2}{\partial \alpha^2} + \delta_{b,s}^2 \frac{\partial^2}{\partial \psi^2} \quad (5)$$

where  $L_\psi = a R_0 B_\theta$  is the radial length of the simulation box in units of  $\psi$ . The quasi-neutrality equation with the approximation  $H_{\text{eq},s}(\psi) = E(1 + \Omega_D \psi) \approx E$  reads as follows [25, 30],

$$\begin{aligned} & \frac{2}{\sqrt{\pi} n_{\text{eq}}(0)} \sum_s Z_s \int_0^1 \kappa \mathcal{K}(\kappa^2) d\kappa \int_0^\infty J_{0,s} f_s \sqrt{E} dE \\ & = \sum_s \frac{e Z_s^2}{T_{\text{eq},s}(0)} \left[ \frac{1 - f_t}{f_t} (\phi - \varepsilon_{\phi,s} \langle \phi \rangle_\alpha) - \bar{\Delta}_s \phi \right], \quad (6) \end{aligned}$$

where,  $n_{\text{eq}}(0)$  is the equilibrium density at  $\psi = 0$ ,  $f_t = \frac{2\sqrt{2\varepsilon}}{\pi}$  is the fraction of trapped particles, which scales as  $\sqrt{\varepsilon}$ , whereas

we consider a constant  $f_i$ .  $\langle \dots \rangle_\alpha$  corresponds to the average on the angle  $\alpha$ . Here passing particles are treated quasi-adiabatically. In all the previous studies of trapped particle modes' instability [8, 25, 26], the gyro-bounce averaged kinetic model was simplified by considering the equilibrium Hamiltonian  $H_{\text{eq}}(\psi) = E(1 + \Omega_D \psi) \approx E$ , which was used to derive the quasi-neutrality equation (6). This approximation is valid only at  $\psi = 0$  and/or  $\Omega_D \ll 1$ . The exact expression for the equilibrium Hamiltonian is,

$$H_{\text{eq}}(\psi, \kappa) = E \left( 1 + \int_0^\psi \Omega_D(\tilde{\psi}, \kappa) d\tilde{\psi} \right) = E \Lambda_D(\psi, \kappa), \quad (7)$$

where  $\Lambda_D(\psi, \kappa) = 1 + \int \Omega_D(\tilde{\psi}, \kappa) d\tilde{\psi}$ , with  $\tilde{\psi}$  is a variable of integration. In the previous derivation of the gyro-bounce averaged Vlasov equation (1) the  $\psi$  derivative of the equilibrium Hamiltonian was considered as  $\frac{dH_{\text{eq}}}{d\psi} = E\Omega_D$ , which remains unchanged for this new Hamiltonian equation (7). Therefore, the expression for the gyro-bounce averaged Vlasov equation (1) remains unchanged. With this new equilibrium Hamiltonian equation (7) the elementary volume in the phase-space can be written as  $d^3v = 4\pi\sqrt{2m}^{-3/2}\sqrt{E}\Lambda_D^{3/2}dE\frac{d\lambda}{4\Omega_D}$ . For simplicity, we consider that the term  $\bar{\Delta}\phi$  associated with the polarization in the quasi-neutrality equation (6) remains unchanged under this new modification in the equilibrium Hamiltonian. By keeping unchanged the right-hand side of the previous quasi-neutrality equation (6) and using the modified expression of elementary volume  $d^3v$  for the integration of the gyro-bounce averaged distribution  $f_s$ , the quasi-neutrality equation can be written as

$$\begin{aligned} & \frac{2\Lambda_D(\psi, \kappa)^{3/2}}{\sqrt{\pi}n_{\text{eq}}(0)} \sum_s Z_s \int_0^1 \kappa \mathcal{K}(\kappa^2) d\kappa \int_0^\infty J_{0,s} f_s \sqrt{E} dE \\ &= \sum_s \frac{eZ_s^2}{T_{\text{eq},s}(0)} \left[ \frac{1-f_i}{f_i} (\phi - \epsilon_{\phi,s} \langle \phi \rangle_\alpha) - \bar{\Delta}_s \phi \right]. \end{aligned} \quad (8)$$

Therefore there is an additional multiplication term  $\Lambda_D(\psi, \kappa)^{3/2}$  that arises in the left-hand side of the previous quasi-neutrality condition equation (6). In this model, the gyro-bounce averaged distribution function  $f_s$  bears four dimensions  $(\alpha, \psi, E, \kappa)$ , and in a further reduced limit of a single  $\kappa$  value it reduces to a three-dimensional (3D) model.

### 2.1. Global linearized model

Considering an initial very small amplitude perturbation of gyro-bounce averaged distribution  $f_s = F_{\text{eq},s} + \tilde{f}_s$  and potential  $\phi = \tilde{\phi}$  in Fourier space as  $\tilde{f}_s = \sum_{n,\omega} f_{s,n,\omega}(\psi, E, \kappa) \exp\{i(n\alpha - \omega t)\}$  and  $\tilde{\phi} = \sum_{n,\omega} \phi_{n,\omega}(\psi) \exp\{i(n\alpha - \omega t)\}$ , then neglecting the higher order nonlinear terms  $\left[ J_{0,s} \tilde{\phi}, \tilde{f}_s \right]_{\alpha,\psi}$ , the linearized form of the Vlasov equation can be written as,

$$\frac{\partial \tilde{f}_s}{\partial t} - \left[ J_{0,s} \tilde{\phi}, F_{\text{eq},s} \right]_{\alpha,\psi} + \frac{\Omega_D E}{Z_s} \frac{\partial \tilde{f}_s}{\partial \alpha} = 0. \quad (9)$$

$n$  and  $\omega$  are the mode number (along  $\alpha$ ), and the angular frequency of the Fourier modes, respectively. Here, we consider

the normalized gyro-bounce averaged equilibrium distribution  $F_{\text{eq},s}$  is Maxwellian energy distribution, which is independent of  $(\alpha, t)$ . Using the new equilibrium Hamiltonian  $F_{\text{eq},s}$  can be written as:

$$F_{\text{eq},s}(\psi, E, \kappa) = \frac{n_{\text{eq},s}(\psi)}{T_{\text{eq},s}^{3/2}(\psi)} \exp\left(-\frac{E\Lambda_D(\psi, \kappa)}{T_{\text{eq},s}(\psi)}\right), \quad (10)$$

where  $T_{\text{eq},s}(\psi)$  and  $n_{\text{eq},s}(\psi)$  are the temperature and density profiles of the equilibrium distribution function of species  $s$ , respectively. In this case, the integration of  $F_{\text{eq}}$  over the velocity space  $d^3v$  leads to  $n_{\text{eq}}(\psi)$ . Hereafter, we denote  $T_{\text{eq}}(\psi)$  as  $T(\psi)$  and  $n_{\text{eq},s}(\psi)$  as  $n_s(\psi)$ . The term  $E\Lambda_D$  allows us to incorporate the radial variation of particle drift velocity. After substituting  $\tilde{f}_s$ ,  $\tilde{\phi}$  and  $F_{\text{eq},s}$  in equation (9), the solution of the Vlasov equation in Fourier space becomes,

$$\begin{aligned} f_{n,\omega} &= \frac{\kappa_n(\psi) + \kappa_T(\psi) \left( \frac{E\Lambda_D(\psi)}{T(\psi)} - \frac{3}{2} \right) - \frac{E\Lambda_D}{T(\psi)} \kappa_\Lambda(\psi)}{Z_s^{-1} \Omega_D(\psi, \kappa) E - \frac{\omega}{n}} \\ &\times \{ J_{0,n,s} \phi_{n,\omega}(\psi) \} F_{\text{eq},s}(\psi, E, \kappa) \end{aligned} \quad (11)$$

where  $\kappa_n(\psi) = \frac{1}{n_s(\psi)} \frac{dn_s}{d\psi}$ ,  $\kappa_T(\psi) = \frac{1}{T_s(\psi)} \frac{dT_s}{d\psi}$  and  $\kappa_\Lambda(\psi) = \frac{1}{\Lambda_D(\psi)} \frac{d\Lambda_D}{d\psi} = \frac{\Omega_D(\psi)}{\Lambda_D(\psi)}$  are the logarithmic gradients of density, temperature and equilibrium Hamiltonian  $H_{\text{eq}}(\psi)$ , respectively.

Considering both electron and ion contributions, the quasi-neutrality condition denoted in equation (8) can be written as,

$$\begin{aligned} & \frac{\sqrt{\pi}}{2T_i(0)} [C_{\text{ad}}(\phi_{n,\omega} - \epsilon_\phi \langle \phi \rangle_\alpha) - C_{\text{pol}} \bar{\Delta} \phi_{n,\omega}] = \mathcal{N}_{n,i} - \mathcal{N}_{n,e}, \\ \mathcal{N}_{n,i} &= \frac{\Lambda_D^{3/2}}{n_i(0)} \int_0^1 \int_0^\infty J_{0,i} f_{i,n,\omega}(\psi, E, \kappa) \sqrt{E} dE \kappa \mathcal{K}(\kappa^2) d\kappa, \\ \mathcal{N}_{n,e} &= \tau \frac{\Lambda_D^{3/2}}{n_e(0)} \int_0^1 \int_0^\infty J_{0,e} f_{e,n,\omega}(\psi, E, \kappa) \sqrt{E} dE \kappa \mathcal{K}(\kappa^2) d\kappa, \end{aligned} \quad (12)$$

where  $\tau = \frac{T_i}{T_e} \Big|_{\psi=0}$ ,  $C_{\text{pol}} = \frac{q_i \omega L_{\psi}}{T_0}$ ,  $C_{\text{ad}} = \frac{1-f_i}{f_i} (1-\tau) C_{\text{pol}}$ ,  $\epsilon_\phi = \frac{\epsilon_{\phi,i} + \tau \epsilon_{\phi,e}}{1+\tau}$  and  $\bar{\Delta} \phi = \bar{\Delta}_i \phi + \tau \bar{\Delta}_e \phi$ . In the limit of a constant *pitch-angle*, the value of  $\Omega_D$  is constant along  $\kappa$ , then the  $\kappa$  integration in equation (12) can be simplified as,  $\int_0^1 \kappa \mathcal{K}(\kappa^2) d\kappa = 1$ . Substituting the value of  $f_{n,\omega}$  from equation (11) in equation (12), the expression of  $\mathcal{N}_s$  becomes

$$\begin{aligned} \mathcal{N}_n &= \frac{\Lambda_D(\psi)^{3/2}}{n_s(0)} \int_0^\infty \sqrt{E} J_{0,n} \left[ \frac{n_s(\psi)}{T^{3/2}(\psi)} \exp\left(-\frac{E\Lambda_D}{T(\psi)}\right) \right. \\ &\times \left. \frac{\kappa_n(\psi) + \kappa_T(\psi) \left( \frac{E\Lambda_D}{T(\psi)} - \frac{3}{2} \right) - \kappa_\Lambda(\psi) \frac{E\Lambda_D}{T(\psi)}}{Z^{-1} \Omega_D(\psi) (E - \chi)} (J_{0,n} \phi_{n,\omega}) \right] dE, \end{aligned} \quad (13)$$

where  $\chi = \frac{\omega}{nZ^{-1}\Omega_D(\psi)}$ , and  $\omega$  have both real and imaginary parts  $\omega = \omega_r + i\gamma$ . Due to the term  $(E - \chi_s)$  in the denominator, there is a possibility of resonance between wave and

particle motion. For ions  $Z_i$  is positive, therefore the resonance occurs only when the phase velocity of the wave has the same sign as the ion precession drift (i.e.  $\omega > 0$ ). By substituting  $\bar{\Delta}_s$  from equation (5) in the left-hand side of the quasi-neutrality condition shown in equation (12), we define the differential operator

$$C_n = \frac{\sqrt{\pi}}{2T_i(0)} \left[ C_{\text{ad}}(1 + \epsilon_\phi \delta_{n,0}) + C_{\text{pol}} \left\{ (\rho_i^{*2} + \tau \rho_e^{*2})(-n^2) - (\delta_{bi}^2 + \tau \delta_{be}^2) \frac{\partial^2}{\partial \psi^2} \right\} \right], \quad (14)$$

where  $\rho_s^* = \frac{q\rho_{e0,s}}{L_\psi}$ , and  $\delta_{n,0}$  is Kronecker delta with the value 1 for  $n=0$  and for  $n \neq 0$ , it is 0. Therefore, the dispersion relation becomes,

$$C_n \phi_{n,\omega} = \mathcal{N}_{n,i}^* \phi_{n,\omega} - \mathcal{N}_{n,e}^* \phi_{n,\omega} \quad (15)$$

where  $\mathcal{N}_{n,s}^* = \frac{\mathcal{N}_{n,s}}{\phi_{n,\omega}}$  is actually a differential operator (equations (4) and (13)) acting on  $\phi_{n,\omega}$ . We will come back to this issue in section 3. Hereafter, we remove the subscript  $\omega$  from  $\phi_{n,\omega}$ , and denote it as  $\phi_n$ , because the linear dispersion relates  $\omega$  to  $n$  values. By substituting the expression of  $C_n$  in equation (15), one can derive a second order linear differential equation of  $\phi_{n,\omega}$  as,

$$\frac{d^2 \phi_n}{d\psi^2} + Q_n(\psi) \phi_n = 0, \quad (16)$$

$$Q_n(\psi) = \frac{\mathcal{N}_{n,i}^* - \mathcal{N}_{n,e}^* - \frac{\sqrt{\pi}}{2T_i(0)} [C_{\text{ad}} + C_{\text{pol}}(\rho_i^{*2} + \tau \rho_e^{*2})n^2]}{\frac{\sqrt{\pi}}{2T_i(0)} C_{\text{pol}}(\delta_{bi}^2 + \tau \delta_{be}^2)}.$$

Considering  $T_i(0) = T_0$ ,  $n_i(0) = n_e(0) = n_0$ , in a normalized unit, these become  $T_i(0) = n_s(0) = 1$ . Here we study the modes for which  $n \neq 0$ , therefore the term  $\epsilon_\phi \delta_{n,0}$  in equation (14) vanishes. For simplicity, to study the TIM instability specifically, we will neglect the electron perturbation  $\tilde{f}_e = 0$  which leads to  $\mathcal{N}_e^* = 0$ . However, the same method is applicable to TEM instability by setting  $\mathcal{N}_i^* = 0$  and  $\mathcal{N}_e^* \neq 0$ . Moreover, for  $\tau \leq 1$ ,  $\rho_i^{*2} \gg \rho_e^{*2}$  and  $\delta_{bi}^2 \gg \delta_{be}^2$ . Therefore, after neglecting those terms associated with electron contribution and substituting  $T_{\text{eq},i} = 1$  in equation (16), the modified expression for  $Q_n(\psi)$  becomes,

$$Q_n(\psi) = \frac{\mathcal{N}_{n,i}^* - \frac{\sqrt{\pi}}{2} [C_{\text{ad}} + C_{\text{pol}} \rho_i^{*2} n^2]}{\frac{\sqrt{\pi}}{2} C_{\text{pol}} \delta_{bi}^2}. \quad (17)$$

The contributions of the density gradient, temperature gradient and the gradient in the equilibrium Hamiltonian are contained in the expression of  $\mathcal{N}_n^*$ . Due to the term  $-\kappa_\Lambda$ , while the increase in the logarithmic gradients of temperature and density  $\kappa_T$  and  $\kappa_n$  help to enhance the TIM instability, the logarithmic gradient of equilibrium Hamiltonian  $\kappa_\Lambda$  helps to stabilize the TIM instability. In the limit  $H_{\text{eq}} \approx E$ , the term  $\kappa_\Lambda = 0$  and  $\Lambda_D = 1$ , in equation (13). Therefore, the growth rate  $\gamma$  of

all the modes  $n$  of TIM instability for the new modified equilibrium Hamiltonian  $H_{\text{eq}}(\psi, \kappa, E)$ , will be significantly smaller compared to the case with the limit  $H_{\text{eq}} \approx E$ . The dispersion relation of the TIM mode instability in the limit of  $H_{\text{eq}} \approx E$  is presented in the appendix. Since the solution in Fourier space equation (11)  $f_{n,\omega} = 0$  for  $n=0$ , the linear analysis is valid only for the mode numbers  $n > 0$ . However, the  $n=0$  mode is linearly stable; it cannot extract free energy from the equilibrium gradients.

## 2.2. Local linearized analysis

The local linear stability analysis of this reduced gyro-bounce averaged model with the new modified equilibrium Hamiltonian can be obtained by expanding  $F_{\text{eq},s}(\psi, \kappa, E)$  equation (10) up to the first order of  $\psi$  around  $\psi = 0$ , and substituting  $\partial_\psi^2 \phi = -k^2 \phi$  (with  $k = \pi$ ) in the dispersion relation, which leads to the new simplified dispersion relation as,  $C_n - \mathcal{N}_{n,i}^* = 0$ . From this, using the Plemelj formula [31], the threshold frequency value of the real part of frequency  $\omega_r$  for TIM instability can be derived as:

$$\omega_r^{\text{new}} = \left( \frac{\frac{3}{2} \kappa_{T0} - \kappa_{n0}}{\kappa_{T0} - \kappa_{\Lambda 0}} \right) \frac{\Omega_{D0}}{\Lambda_D} T_0 n, \quad (18)$$

where the subscript '0' denotes the variables' value at  $\psi = 0$ . Here, we restrict the analysis to the case of resonant interactions only, i.e.  $\omega_r > 0$ ; hence, equation (18) is valid for the cases with  $(3\kappa_T/2 - \kappa_n)/(\kappa_T - \kappa_\Lambda) > 0$ . The threshold value of  $\kappa_T$  for the instability can be written as

$$\kappa_{T,\text{th}}^{\text{new}} = \frac{C_n \Omega_{D0}}{\Lambda_{D0} \int_0^\infty \mathcal{J}_{0,n}^2 \exp(-\xi) \sqrt{\xi} d\xi} + \kappa_{\Lambda 0} \quad (19)$$

where  $\xi = \frac{E\Lambda_D}{T}$ . The threshold values of  $\omega_r$  and  $\kappa_T$  equations (A5) and (A6) in the limit of  $H_{\text{eq}} \approx E$  [9] can be recovered by substituting  $\Lambda_D = 1$  and  $\kappa_\Lambda = 0$  in equations (18) and (19). The relation between these two threshold  $\kappa_T$  values is

$$\kappa_{T,\text{th}}^{\text{new}} = \frac{\kappa_{T,\text{th}}}{\Lambda_{D0}} + \kappa_{\Lambda 0}, \quad (20)$$

where  $\kappa_{T,\text{th}}^{\text{new}}$  and  $\kappa_{T,\text{th}}$  are the threshold values of  $\kappa_T$  for TIM instability in the case with  $\kappa_\Lambda$  and without  $\kappa_\Lambda$ , respectively. For  $\Lambda_{D0} \approx 1$ ,  $\kappa_{T,\text{th}}^{\text{new}} \gg \kappa_{T,\text{th}}$ , which suggests that a relatively strong gradient in the temperature profile is required in order to obtain TIM instability, compared to the case with  $H_{\text{eq}} \approx E$ . In case of adiabatic electron response there is a non-resonant branch of TIM for  $\chi < 0$  [25]. But here we are focusing only on the resonant branch of TIM, for which  $\chi > 0$ .

In the present study, unlike the local linear analysis, instead of Taylor expansion of  $F_{\text{eq},s}$  around  $\psi = 0$ , a full  $\psi$  dependent Maxwellian distribution for the equilibrium gyro-bounce averaged particle distribution  $F_{\text{eq},a}(\psi, \kappa, E)$  is considered. Therefore, using this global linear analysis, the effects of any type of temperature, density and precession frequency profiles on the stability of TIMs can be investigated. In the next section, we will solve the differential equation of  $\phi$  equation (16) with

the expression for  $Q_n$  from equation (17) using the spectral method.

### 3. Global linear analysis: spectral method

The  $Q_n$  function in equation (17) depends on  $\psi$  in an intricate manner. However, in the limit of local linear analysis [9],  $Q_n$  is independent of  $\psi$ . Therefore  $-Q_n$  becomes the eigenvalue of the operator  $\partial_\psi^2$  in equation (16). However, in our global linear analysis, due to the full Maxwellian distribution  $F_{\text{eq}}$ , it is impossible to eliminate the  $\psi$  dependency in  $Q_n$ , i.e.  $-Q_n$  is no more an eigenvalue of  $\partial_\psi^2$ . Here we use a spectral approach [28, 29, 32] to solve equation (16). We can consider our co-ordinate system  $(\psi, \alpha)$  as a polar co-ordinate system with  $\psi$  as radial axis and  $\alpha$  as angular axis. If we consider the solution  $\phi(\psi, \alpha)$  as a scalar analytic function in the region  $0 \leq \psi \leq 1$ , according to the theorem-1 of the page 374 in [32], using a spectral approach the solution  $\phi(\psi, \alpha)$  can be expanded as:

$$\phi(\psi, \alpha) = \sum_{n=-\infty}^{\infty} \psi^{|n|} \sum_{m=1}^{\infty} \hat{\phi}_{n,m} \mathfrak{F}_m(\psi) \exp(in\alpha) \quad (21)$$

where  $\mathfrak{F}_m(\psi)$  is an even power function of  $\psi$ , and the sum index  $m$  has values  $m = 1, 2, \dots, \infty$ . In practice, a truncation is performed so that it is limited to the first  $M$  number functions of  $\mathfrak{F}_m$ . In equation (16) all the differentiation in  $\alpha$  is taken in Fourier-space. Therefore, according to the spectral approach from equation (21) the solution of equation (16)  $\phi_n(\psi)$  can be expressed as:

$$\phi_n(\psi) = \psi^{|n|} \sum_{m=1}^M \hat{\phi}_{n,m} \mathfrak{F}_m(\psi). \quad (22)$$

The boundary conditions for  $\phi_n(\psi)$  in equation (16) are  $\phi|_{\psi=0} = 0$  and  $\phi|_{\psi=1} = 0$ . Our first choice for  $\mathfrak{F}_m$  was  $\mathfrak{F}_m = (1 - \psi^2)\psi^{2(m-1)}$ , but this choice gives poorly conditioned matrices. For good condition matrices, the coefficients  $\hat{\phi}_{n,m}$  go down towards zero exponentially with increasing  $m$  and at  $m = M$ ,  $\hat{\phi}_{n,M} \approx 0$ . Then, we consider orthogonal polynomials, Chebyshev polynomials of first kind  $T_{2(m-1)}(\psi)$ , for constructing  $\mathfrak{F}_m$  as:

$$\mathfrak{F}_m(\psi) = (1 - \psi^2)T_{2(m-1)}(\psi) \quad (23)$$

which were used for studying the collisional drift wave and ITG instabilities in a cylindrical plasma, using the spectral method [28, 29]. However, in the case of TIM instability, we found that this choice of function gives good condition matrices for lower values of  $n$ . For higher values of  $n$ , the coefficients  $\hat{\phi}_{n,m}$  do not go down towards zero exponentially with increasing  $m$ . Then, we choose  $n = 1$  for the factor  $\psi^{|n|}$ , in the expansion function equation (22) and the dependency of the solution on the mode-number  $n$  is entirely determined by the expression  $Q_n$  in equation (16). With this new choice, the coefficients  $\hat{\phi}_{n,m}$  go down towards zero exponentially with increasing  $m$ . Moreover, we have checked that using this new choice of expansion function, one can recover the solutions of the collisional drift wave instability study, as given in [28, 29].

By defining  $C_m = \psi \mathfrak{F}_m$  the expression of  $\phi_n(\psi)$  can be written as,

$$\phi_n(\psi) = \sum_{m=1}^M \hat{\phi}_{n,m} C_m. \quad (24)$$

Here  $C_m = \psi(1 - \psi^2)T_{2(m-1)}(\psi)$ . Using this new choice of  $\phi_n(\psi)$  rather good conditioning properties of matrices are obtained for large values of  $n$  in our study. Substituting the value of  $\phi$  in equation (16) we get,

$$\sum_{m=1}^M \hat{\phi}_{n,m} \frac{d^2 C_m(\psi)}{d\psi^2} = - \sum_{m=1}^M \hat{\phi}_{n,m} Q_n(\psi) C_m(\psi), \quad (25)$$

where  $m$  is the index of the spectral function  $C_m$ , and  $n$  is the wave number of TIM instability along the toroidal precession angle  $\alpha$ . The second-order differential equation (25) is solved numerically. By proceeding this way, equation (25) is only solved at the points  $\psi$ , where its left hand side is vanishing for the first dropped higher order term of the expansion, namely the term  $C_{M+1}(\psi) = \psi(1 - \psi^2)T_{2M}(\psi)$ . Those  $\psi$  values are called the collocation points, which are defined by the  $M$  zeros of the Chebyshev polynomial  $T_{2M}(\psi)$  situated in the interval  $0 \leq \psi \leq 1$ , i.e.  $\psi_l = \cos\left(\frac{(2l-1)\pi}{4M}\right)$  for  $l \in \{1, \dots, M\}$ . Since  $C_{M+1}$  vanishes at these  $\psi$  locations, for  $J_0 = 1$  the right hand side of equation (25) also vanishes at  $m = M + 1$ . Moreover, for gyro-bounce average operator  $J_0$  according to equation (4) we solve the equation (25) iteratively where the operator  $\mathcal{N}_n^*$  inside  $Q_n(\psi)$  is applied on a solution  $\phi_{n-\Delta n}(\psi)$  which is obtained from the previous iteration. Therefore, at any iteration  $Q_n(\psi)$  is a known function of  $\psi$ ; it does not directly operate on  $C_m$ . Hence, at the collocation points the right hand side of equation (25) vanishes for the  $m = (M + 1)$ . To minimize the truncation error, the discretization in  $\psi$  is considered at those collocation points. We will explain this iteration method at the end of this section. For each value of wave number  $n$  along  $\alpha$ , equation (25) is evaluated at these collocation points and yields the matrix problem,

$$\mathcal{M}_D \hat{\phi}_n = -\mathcal{M}_Q \hat{\phi}_n \quad (26)$$

where  $\hat{\phi}_n = \begin{pmatrix} \hat{\phi}_{n,1} \\ \vdots \\ \hat{\phi}_{n,M} \end{pmatrix}$  is the vector representing the solution, and the matrices are,

$$(\mathcal{M}_D)_{l,m} = \frac{d^2}{d\psi_l^2} C_m(\psi_l), \quad (27)$$

$$(\mathcal{M}_Q)_{l,m} = Q_n(\psi_l) C_m(\psi_l), \quad (28)$$

with  $l, m \in \{1, \dots, M\}$ . We then scan the  $(\omega_r, \gamma)$  plane (where  $\omega = \omega_r + i\gamma$ ), and search for values of  $\omega$  such that one eigenvalue of the matrix  $\mathcal{M} = \mathcal{M}_D + \mathcal{M}_Q$  vanishes within machine precision. During this search, there is no restriction on the range of  $\omega_r$  values, and we search only for positive  $\gamma$  values. For this purpose, a method that finds the minimum of a scalar

function of several variables, starting at an initial guess value, and which iterates using the *simplex search* method [33] is used. Then, using the eigenvector of matrix  $\mathcal{M}$  associated with this smallest eigenvalue, the electric potential  $\phi_n(\psi)$  can be constructed using equation (24). The solution  $\phi_n(\psi)$  has both real and imaginary parts. The *spectral-convergence* or rate of change of the coefficient  $\hat{\phi}_{n,m}$  values with different  $M$  values depends on the nature of the matrix  $\mathcal{M}_Q$ . Usually, acceptable smooth  $\hat{\phi}_{n,m}$ s follows exponentially decaying functions with  $m$ , i.e.  $\hat{\phi}_{n,m} = \hat{\phi}_{n,0} \exp(-|\beta|m)$ , where  $\beta$  is a constant. For different initial guess values, the minimum searching method can converge toward different values of  $\omega$ . Among these solutions, one finds the couple  $(\omega_r, \gamma)$  for which the instability growth rate  $\gamma$  is maximum. We will take that particular set as a solution  $(\omega_r, \gamma)$ . To generate the curve  $(\omega_r$  versus  $n$ ) and  $(\gamma$  versus  $n$ ) we start from mode  $n = 1$  and search for the highest value of growth rate, by choosing different initial guess values as  $\omega_{r0} \in [0, 3\omega_{rL}]$  and  $\gamma_0 \in [0, \omega_{rL}]$  (since  $\omega_r \geq \gamma$ ), and with the intervals  $\Delta\omega_{r0} = 0.1\omega_{rL}$ ,  $\Delta\gamma_0 = 0.01\omega_{rL}$ , where  $\omega_{rL}$  is the threshold value of  $\omega_r$  obtained from the local linear analysis equation (18). In fact, the range and the intervals for the initial guess values depend on the nature of the instability, i.e., on the matrix  $\mathcal{M}_Q$ . After finding the highest value of growth rate for  $n = 1$ , increase the  $n$  value slowly with a step  $\Delta n = 0.1$ . Although the mode numbers  $n$  along  $\alpha$ , are integer numbers, there is no such restriction on  $n$  for solving the differential equation (25) for fractional values of  $n$ . In the search method, we choose the solution  $\omega$  of  $n - \Delta n$  step, as an initial guess  $(\omega_{r0}, \gamma_0)$  value to search the solution for mode number  $n$ . Here, we consider that the  $(\omega_r$  versus  $n$ ) and  $(\gamma$  versus  $n$ ) profiles vary smoothly with  $n$ , such that a small change in  $n$ , changes the  $\mathcal{M}$  matrix by a small amount, and helps to find-out the values  $(\omega_r, \gamma)$  close to the initial guess value  $(\omega_{r0}, \gamma_0)$ , and keep the solutions within the same branch with the highest growth rate. A larger step in  $\Delta n$  in the searching method, may lead to a departure of the solution  $(\omega_r, \omega_i)$  from the branch with the highest growth rate. However, if the solution departs from any particular branch, i.e. if it leads to a sudden change in the potential profile for two consecutive  $n$  values, then one has to decrease the  $\Delta n$  value.

The main difficulty for solving equation (16) using the spectral method is to construct the  $Q_n(\psi)$  matrix. To calculate  $\mathcal{N}_{n,i}^*$ , the gyro-bounce average operator  $J_{0,n,i}$  is applied to the potential solution  $\phi_n$  in equation (13), which is an unknown quantity of equation (16). Therefore, we will solve equation (16) for  $\phi$  iteratively. Moreover, to calculate the gyro-bounce average of any function  $\mathcal{F}(\psi)$  using the Padé expression equation (4), we solve the differential equation,

$$\left(1 - \frac{E}{T(0)} \frac{\delta_{b0,s}^2}{4} \frac{d^2}{d\psi^2}\right) \bar{\mathcal{F}}(\psi) = \left(1 + \frac{E}{T(0)} \frac{\rho_*^2}{4} n^2\right)^{-1} \mathcal{F}(\psi), \quad (29)$$

where,  $\mathcal{F}$  is a known function, on which the gyro-bounce average operator  $J_0$  is applied and generates the gyro-bounce averaged quantity  $\bar{\mathcal{F}}$ . We solve equation (29), using the spectral

method with the boundary condition  $\bar{\mathcal{F}} = 0$  at  $\psi = 0$  and  $\psi = L_\psi = 1$ . Finally, equation (16) is solved iteratively, by calculating  $\mathcal{N}_n$  for the  $\phi_n$  solution from the previous iteration. For the first iteration with mode number  $n$ , the potential solution  $\phi_{(n-\Delta n)}(\psi)$  of the mode  $n - \Delta n$  is taken into account to calculate  $\mathcal{N}_n$ . However, for the calculation with mode  $n = 1$ , at the beginning (first iteration) the potential solution is not available, therefore at first, equation (16) is solved using the spectral method for the case with  $J_{0,s} = 1$  and constructs the potential using equation (24). The gyro-bounce average operator equation (4) is then applied on that potential solution for calculating  $\mathcal{N}_n$  at the first iteration for  $n = 1$ , and constructs the solution  $\phi_n$ . In the next iteration, this  $\phi_n$  is used to calculate  $\mathcal{N}_n$  and update the solution  $\phi_n$ . After each iteration,  $\Delta\phi_n$ , the difference in the solution  $\phi_n$  from its value at the previous iteration, is calculated and this iteration method continues until the accuracy limit  $|\Delta\phi_n| \sim 10^{-3}$  is achieved.

Although this solver based on the spectral method is quite robust for studying the linear stability of the TIM for different dependent parameters (temperature, density and precession frequency) profiles, it has some limitations. We have observed that this spectral method can calculate the  $(\gamma, \omega_r)$  precisely for temperature profiles having  $\kappa_T < 10\kappa_{T,\text{th}}$ , and beyond that the method becomes unstable, and even a very small change in  $\Delta n < 0.001$  departs the solution from the expected branch with the highest growth rate.  $\kappa_{T,\text{th}}$  is the threshold value of instability which is given by equations (19) and (A6). For  $H_{\text{eq}} \approx E$  and  $\kappa_n = 0$ , the threshold value is  $\kappa_{T,\text{th}} \sim 0.12$  for the mode number  $n = 1$  [9]. Moreover, this method can be applied only for the potential solutions which have zero values at the boundary ( $\phi = 0$  at  $\psi = 0$  and  $\psi = 1$ ). In the next two sections 4 and 5, this spectral technique is used to study the effect of temperature and precession frequency profiles (having  $\kappa_{T,\text{max}} < 10\kappa_{T,\text{th}}$ ) on TIM instability for the case in the limit  $H_{\text{eq}} \approx E$  and for the exact equilibrium Hamiltonian  $H_{\text{eq}}(\psi, \kappa, E)$ .  $\kappa_{T,\text{max}}$  is the maximum value of a  $\kappa_T(\psi)$  profile.

#### 4. Effect of temperature and precession frequency on TIM instability in the limit $H_{\text{eq}} \approx E$

In this section, we consider the case with the limit  $H_{\text{eq}} \approx E$  and present the effect of different temperature profiles, and different precessional frequency profiles  $\Omega_D(\psi, \kappa)$ , corresponding to different safety factor profiles, on the TIM instability. We can substitute  $\Lambda_D = 1$  and  $\kappa_\Lambda = 0$  in the equation (13) and get the required expression for the  $\mathcal{N}_n$  equation (A3), in the limit  $H_{\text{eq}} \approx E$ . In this limit, the growth rate mostly depends on the terms  $\kappa_T$  and  $\kappa_n$  in equation (13). Moreover, for all the cases the results from the global linear analysis are compared with the linear TERESA simulations. Throughout this paper, we have considered a flat density profile  $\kappa_n = 0$ , which prevents the generation of electron roots of TIM ( $\omega_r < 0$ ) with propagation along the electron diamagnetic direction (appendix of [34]). Here all the modes are ion roots of the TIM which propagate along the ion diamagnetic direction. In this sense the modes are ‘pure-TIM’.

#### 4.1. Different temperature profiles

In this section 4.1 we use four different types of temperature profiles and a flat density profile  $\kappa_n = 0$ , and investigate their effect on the TIM instability. These temperature profiles are presented as,

$$\begin{aligned}
 T_1(\psi) &= T_0(1 + G_T\psi) \\
 T_2(\psi) &= T_0 + \frac{G_T}{2} \left( 1 + L_1 \left[ \log \left( \cosh \frac{\psi - \psi_1}{L_1} \right) \right. \right. \\
 &\quad \left. \left. - \log \left( \cosh \frac{\psi - (1 - \psi_1)}{L_1} \right) \right] \right) \\
 T_3(\psi) &= T_0 \exp(G_T\psi) \\
 T_4(\psi) &= T_0 \exp \left[ G_T R_T \tanh \frac{\psi^2 - \psi_1^2}{R_T^2} \right].
 \end{aligned} \tag{30}$$

Here we use the constant parameters  $T_0 = 1$ ,  $G_T = 0.25$ ,  $L_1 = 0.025$ ,  $\psi_1 = 0.2$ ,  $R_T = 0.5$  and for the temperature profile  $T_4$  we have chosen two different values of  $\psi_1$ , (0.2 and 0.5). Figure 1 presents all these five different temperature profiles.  $T_1(\psi)$  is the temperature profile with a constant temperature gradient.  $T_2(\psi)$  has a constant gradient inside the simulation domain from  $0.2 \leq \psi \leq 0.8$ . The width of this region is controlled by the parameter  $\psi_1$  in  $T_2$ . Near the boundary, the gradient is zero along the  $\psi$  direction. Therefore, there is a sudden change in gradient at  $\psi = 0.2$  and  $0.8$ . This type of profile with zero gradient at the boundary is used in the TERESA simulation to prevent numerical instabilities arising from the boundaries.  $T_3(\psi)$  is an exponentially increasing temperature profile.  $T_4(\psi)$  is a special type of temperature profile which has zero gradient near the boundary, and inside the box it has a finite gradient which can be controlled by the parameter  $\psi_1$  keeping  $G_T$  constant. Here, two different values of  $\psi_1$  are used:  $\psi_1 = 0.2$  and  $\psi_1 = 0.5$ . For both values of  $\psi_1$  the gradient changes smoothly from zero to a finite value as  $\psi$  goes from the boundary toward the center region. Therefore, this profile has less-chance to generate numerical instabilities. Temperature  $T_i$  is normalized to  $T_0$ , and the poloidal magnetic flux is normalized such that  $\psi = 0$  is close to the last-closed flux surface and  $\psi = 1$  is in the core region of the tokamak. Therefore  $T_i = 0.9$  is associated with the ion temperature  $0.9T_0$ . Moreover, for any particular temperature profile, as an example  $T_1$ , the core-most temperature ( $\psi = 1$ ) is  $1.25T_0$  and the temperature at the edge ( $\psi = 0$ ) is  $T_0$ , so that  $\psi \in [0, 1]$  corresponds to a limited radial extent of the tokamak where the temperature changes by only 25%. In tokamak experiments, the ion temperature profile depends on the operation-mode; during L-mode operation it looks like a bell shaped profile with a flat top near the core and decreases toward the scrape-off layer region, while during H-mode operation, due to the generation of an edge transport barrier, the plasma temperature profile changes significantly. It is difficult to present the entire temperature profile using a single function, but the profiles  $T_1$ ,  $T_2$ ,  $T_3$  and  $T_4$  are somewhat representative of radial sections as we have checked from different tokamak experiments, e.g., data from JET [3, 35] and COMPASS [36].

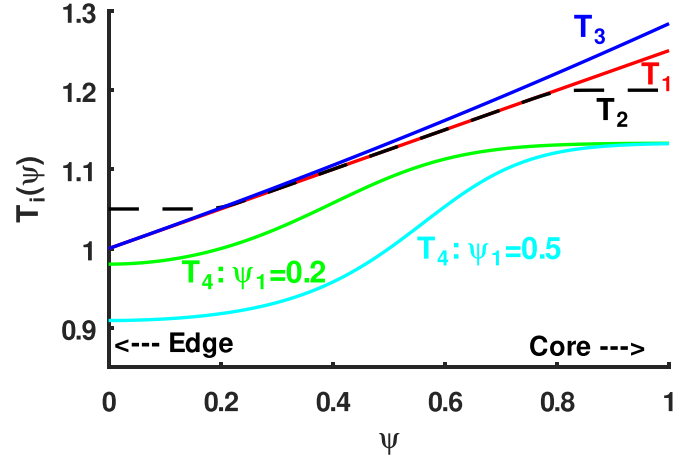


**Figure 1.** Five different types of temperature profile:  $T_1(\psi)$  (red solid line),  $T_2(\psi)$  (black dashed line),  $T_3(\psi)$  (blue solid line),  $T_4(\psi)$  with  $\psi_1 = 0.2$  (green solid line) and  $T_4(\psi)$  with  $\psi_1 = 0.5$  (cyan solid line). The radial interval in-between the LCFS and the very core region of a tokamak, respectively.  $\rightarrow \rightarrow$  near  $\psi = 1$ : indicates the direction towards the core region of the tokamak.  $\leftarrow \leftarrow$  near  $\psi = 0$ : indicates the direction towards the edge region (LCFS) of the tokamak.

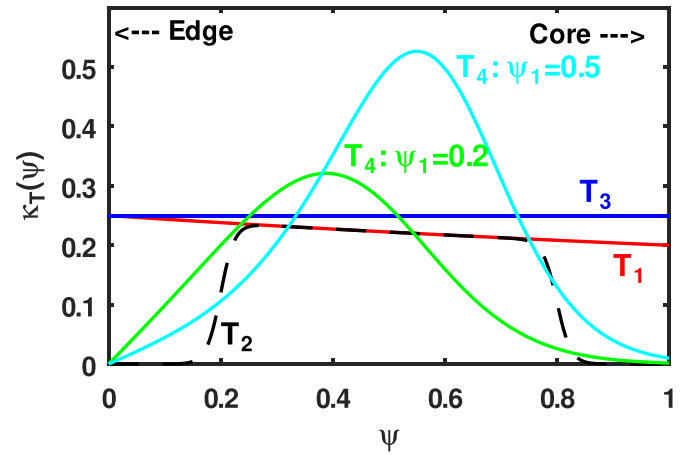


**Figure 2.**  $\kappa_T = \frac{d \log T(\psi)}{d\psi}$  profiles for the five different temperature profiles.

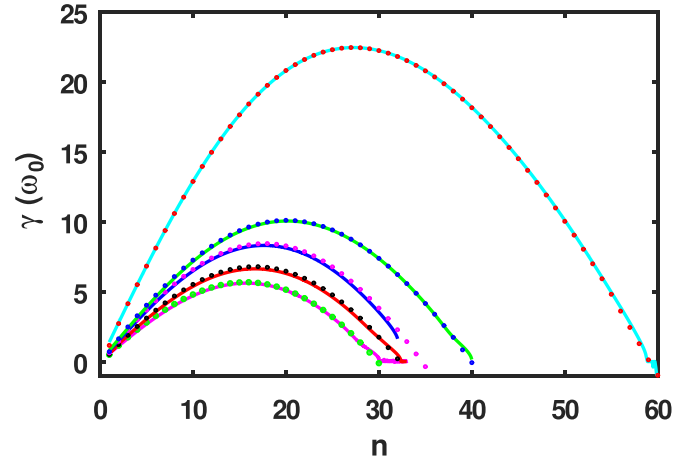
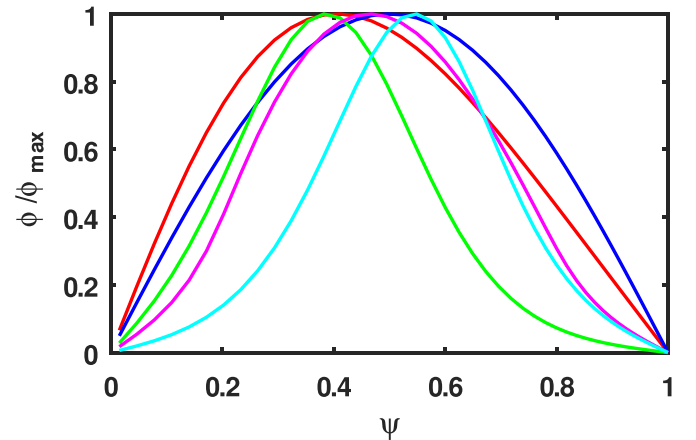
Figure 2 presents the  $\kappa_T(\psi) = \frac{1}{T(\psi)} \frac{dT}{d\psi}$  profiles for all these five temperature profiles. The  $\kappa_T$  profiles change significantly for all five temperature profiles. The temperature profile  $T_4$  with  $\psi_1 = 0.5$  and  $0.2$  has  $\kappa_T$  profiles with peak values  $0.53$  at  $\psi \approx 0.6$  and  $0.31$  at  $\psi \approx 0.4$ , respectively and then gradually decreases to zero toward the boundaries. The exponential temperature profile  $T_3$  has a constant  $\kappa_T$ . Profiles  $T_1$  and  $T_2$  have exactly similar  $\kappa_T$  profiles,  $\kappa_T \propto \psi^{-1}$  within the region  $0.2 \leq \psi \leq 0.8$ , and near the boundaries  $\psi < 0.2$  and  $\psi > 0.8$ ,  $\kappa_T$  suddenly jumps to zero for  $T_2$ . Therefore in  $T_2$ , the TIM instability arises due to the temperature profile within  $0.2 \leq \psi \leq 0.8$ .

**4.1.1.  $J_0 = 1$  case.** Since the case with gyro-bounce average operator  $J_0 = 1$  is numerically the simplest case, we first validate our global linear analysis for the case with  $J_0 = 1$  and with five different temperature profiles. Moreover, for mode

number  $n = 1$ , the potential solution from the  $J_0 = 1$  case will be used to calculate  $\mathcal{N}_n$ . The other main parameters which are used in this study are presented in table 2. The growth rate  $\gamma$  of TIM instability for different mode numbers  $n$  is presented in figure 3 for all the five temperature profiles. This spectral method is also able to find out the negative growth rates for the higher mode numbers. Since we are interested only in the unstable TIMs with positive growth rates ( $\gamma > 0$ ), in all the figures of  $\gamma - n$  profiles, only the modes with  $\gamma > 0$  are presented. For the temperature profile  $T_4$  with  $\psi_1 = 0.5$ , the effective temperature gradient and hence the parameter  $\kappa_T$  has the highest value compared to other temperature profiles. Therefore, as expected, the growth rate of the TIM instability is higher compared to the other cases. For the other temperature profiles, the growth rate decreases as the effective value of  $\kappa_T$  decreases. The growth rate of the highest growing mode for the temperature profiles  $T_4$  with  $\psi_1 = 0.5$ ,  $T_4$  with  $\psi_1 = 0.2$ ,  $T_3$ ,  $T_2$  and  $T_1$  are 22.5, 10, 8.3, 5.6 and 6.6 $\omega_0$ , respectively, and the location of the most unstable modes are  $n \approx 27$ , 20, 17, 15 and 16, respectively. Therefore, even for the gyro average operator  $J_0 = 1$  case the growth rate of the TIM instability strongly depends on the temperature profile, and the mode with the highest growth rate shifts toward zero with decreasing value of  $\kappa_T$ . For low mode numbers, the growth rate increases with increasing  $n$ . At very high  $n$  (after the mode with highest growth rate), the growth rate decreases and goes down to zero due to the presence of the polarization drift term within the model, and finally generates a bell-shaped growth-rate profile. Moreover, the presence of gyro-average operator  $J_0$  according to equation (4), will enhance this effect, which decreases the growth rate further for higher mode numbers—this is presented in the next section, 4.1.2. All the growth-rate profiles at large values of mode-number  $n$ , where  $\gamma \rightarrow 0$  and  $\omega_r$  has very large values ( $\omega_r \gg \gamma$ ), slightly depart from the expected trend. The reason for this is that the integration of equation (13) for calculating  $\mathcal{N}_n$  is a contour integration, and in the complex plane the contour/path of the integration depends on the sign of the imaginary part of  $\chi$  i.e.  $\gamma$ . Since we are interested in the modes with  $\gamma > 0$ , we have considered the integration path for the pole at  $E = C(\omega_r + i\gamma)$ , where  $C = (n\Omega_D)^{-1}$ . For negative values of  $\gamma$  and  $\gamma = 0$  the contours of the integration will be different because the poles are situated at  $E = C(\omega_r - i\gamma)$  and  $E = C\omega_r$ , respectively. One has to take into account these new contours to get the exact values of growth rate when  $\gamma \rightarrow 0$  and  $\gamma \leq 0$ . However, for higher  $\omega_r$  the phase velocity of the wave is very high, and the kinetic effect of trapped ions to TIMs is negligible. Therefore, the growth rate of those modes is left out of our present study. The dots on the growth-rate curves present the measured growth rates of the different modes  $n$  for different temperature profiles from the linear TERESA simulation with  $J_0 = 1$ . These good agreements of the growth-rate profiles validate the accuracy of our spectral method to the semi-Lagrangian based Vlasov simulation results. In order to generate an entire ( $\gamma$  versus  $n$ ) curve, our spectral method based solver takes only 10–15 min for  $J_0 = 1$  and 20–30 min for  $J_0$  according to the Padé expression, whereas a serial version of the TERESA simulation takes around 16 h. Figure 4 presents the potential solution  $\phi_n(\psi)$  profiles for  $n = 1$  for

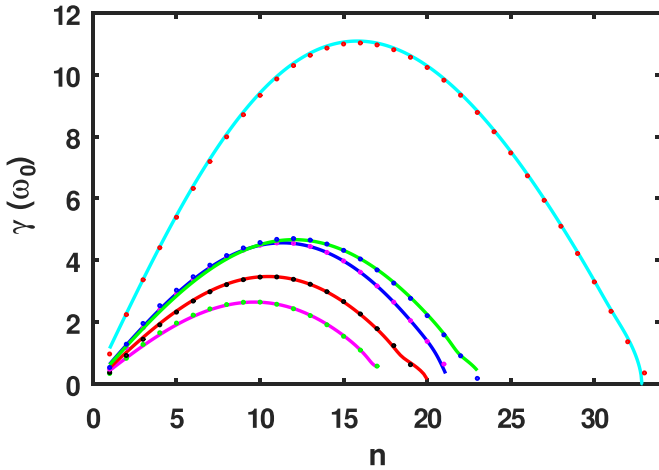
**Table 2.** Main input parameters used for studies in section 4.1.

$\delta_{b,i}$	$\rho_{c,i}$	$C_{ad}$	$C_{pol}$	$\Omega_D$	$T_{eq}$	$n_{eq}$	$M$	$G_T$
0.1	0.03	0.1	0.1	1	1	1	50	0.25


**Figure 3.** Growth rate  $\gamma$  versus mode number  $n$  profiles with  $J_0 = 1$ , for the five different temperature profiles:  $T_4(\psi)$  with  $\psi_1 = 0.5$  (cyan line),  $T_4(\psi)$  with  $\psi_1 = 0.2$  (green line),  $T_3(\psi)$  (blue line),  $T_1(\psi)$  (red line) and  $T_2(\psi)$  (magenta line). The dots denote the results from the linear TERESA simulation with  $J_0 = 1$ . Each set of dots marked by the same color is from a single simulation.

**Figure 4.** Potential solutions  $|\phi_n(\psi)|/\phi_{\max}$  for mode  $n = 1$  with  $J_0 = 1$  for the temperature profiles:  $T_4(\psi)$  with  $\psi_1 = 0.5$  (cyan line),  $T_4(\psi)$  with  $\psi_1 = 0.2$  (green line),  $T_1(\psi)$  (red line),  $T_2(\psi)$  (magenta line), and  $T_3(\psi)$  (blue line).

the different temperature profiles. Depending on the  $\kappa_T$  profiles, different  $\phi_n(\psi)$  profiles are generated. Since the potential solution has both real and imaginary parts, for all the potential profiles within this paper, we take its absolute values and then normalize by its maximum value. All the results that are presented hereafter use the gyro-bounce average operator according to the Padé expression equation (4).

**4.1.2.  $J_0$  according to the Padé expression.** After validating the  $J_0 = 1$  case, we intend to solve the differential equation (16) by calculating  $\mathcal{N}_n$  from equation (A3) with



**Figure 5.**  $\gamma$  versus  $n$  profiles with  $J_0$  equation (4) for the five different temperature profiles:  $T_4(\psi)$  with  $\psi_1 = 0.5$  (cyan line), and  $T_4(\psi)$  with  $\psi_1 = 0.2$  (green line),  $T_3(\psi)$  (blue line),  $T_1(\psi)$  (red line) and  $T_2(\psi)$  (magenta line). The dots denote the results from the linear TERESA simulation.

the Padé expression for the gyro-bounce average operator  $J_0$  equation (4). The gyro-bounce averaged quantity ( $J_0 f_n$  and  $J_0 \phi_n$ ) is calculated by solving the differential equation (29) using the spectral method. First  $J_{0,n} \phi_{n,\omega}$  is calculated using the solution  $\phi_n$ , calculated from equation (16) by implementing  $J_0 = 1$ . Then we use this gyro-bounce averaged potential  $\bar{\phi} = J_{0,n} \phi_{n,\omega}$  in equation (A2) to construct the particle distribution  $f_n$ , and finally the gyro-bounce averaged distribution function  $\bar{f}_n$  is obtained similarly by solving the differential equation (29) which is used to calculate  $\mathcal{N}_n$ . Figure 5 presents the growth rate of different modes  $n$  of TIM instability, for the five different temperatures profiles equation (30). In comparison with the previous  $J_0 = 1$  cases, the gyro-bounce averaged operator decreases the growth rate  $\gamma$  of the TIM instability by a significant amount for all the temperature profiles, roughly by a factor of two in terms of the highest growth rate. Also, the modes with the highest growth rate for each temperature profile are different from the previous  $J_0 = 1$  case and they are shifted toward lower mode numbers. Therefore the gyro-average operator reduces the instability of the TIMs compared to the  $J_0 = 1$  case. However, the effect of the variation in temperature profiles on their growth rate remains unchanged. Similar to the previous  $J_0 = 1$  case, the growth rate of TIMs depends on the  $\kappa_T$  value, and the profile  $T_4$  with  $\psi_1 = 0.5$  generates the highest growth rate, which decreases as the  $\kappa_T$  value decreases for the other temperature profiles. Each dot with different colors on the solid lines presents the growth rate of different modes  $n$  for different temperature profiles from the linear TERESA simulation using the Padé expression for the gyro-bounce average operator. Figure 6 presents the frequency  $\omega_r$  (real part) of different TIMs  $n$  for five different temperature profiles. For the lower mode numbers  $n \leq 10$  frequencies  $\omega_r$  are almost similar for all the temperature profiles. The black dashed line presents  $\omega_r = \frac{3}{2}n$  which is the solution of the local linear analysis equation (A5) in the limit of  $\psi \rightarrow 0$  [9]. Therefore, the frequencies  $\omega_r$  of TIMs are higher

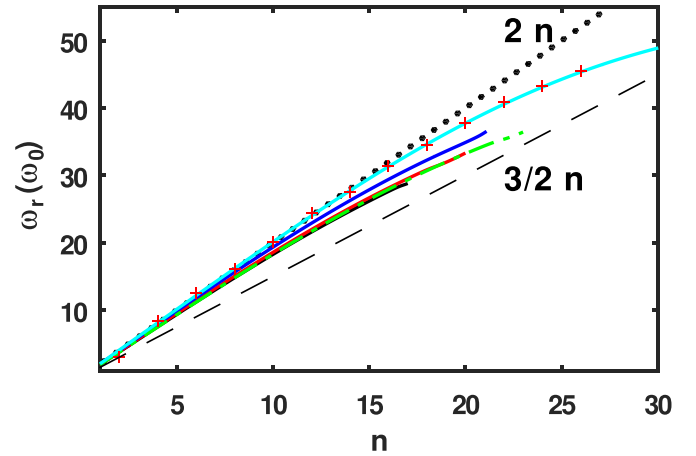


**Figure 6.** Real part of TIM frequency  $\omega_r$  versus mode-number  $n$  with  $J_0$  equation (4) for five different temperature profiles:  $T_4(\psi)$  with  $\psi_1 = 0.5$  (cyan line),  $T_4(\psi)$  with  $\psi_1 = 0.2$  (dashed green line),  $T_2(\psi)$  (black line),  $T_1(\psi)$  (red line) and  $T_3(\psi)$  (blue line). The red+ marker presents the linear TERESA simulation results for  $T_4$  with  $\psi_1 = 0.5$ . The dashed black line presents  $\omega_r = 3/2n$ , and the black dotted line presents  $\omega_r = 2n$ .

compared to the local linear case. Indeed, we found for these cases that they follow the  $\omega_r \sim 2n$  relation for the global linear analysis. The red marker '+' presents the results from the linear TERESA simulation for the temperature profile  $T_4$  with  $\psi_1 = 0.5$ . Figure 7 presents the potential solutions  $\phi_n(\psi)$  of equation (16) for  $n = 1$ , for all the five different temperature profiles. The potential profiles are slightly different from the previous case with  $J_0 = 1$  (figure 4), due to the gyro-bounce average operator  $J_0$  equation (4). Figure 8 shows the  $\phi_n(\psi)$  solution profile equation (24) of mode number  $n = 15$  for the temperature  $T_4$  with  $\psi_1 = 0.5$ , which is almost similar to the mode number  $n = 1$  (cyan line in figure 7). The dashed black line presents the potential profile from the linear TERESA simulation for the temperature profile  $T_4$  with  $\psi_1 = 0.5$  and mode number  $n = 15$ . The potential solution is also in good agreement with the TERESA simulation. Figure 9 presents the decimal logarithms of the coefficients  $\hat{\phi}_{n,m}$  of the function  $C_m$  in equation (24) for the mode number  $n = 15$  for the case with temperature profile  $T_4(\psi_1 = 0.5)$ . The coefficients  $\hat{\phi}_{n,m}$  decrease as  $m$  increases. This confirms the spectral convergence of  $\hat{\phi}_{n,m}$ , which follows  $|\hat{\phi}_{n,m}| \sim A \exp(-\beta m)$ , with  $\beta = 0.7$  for  $1 \leq m \leq 18$  (red dashed line in figure 9). Note that  $|\hat{\phi}_{n,m}/\hat{\phi}_{n,1}| < 10^{-5}$  for  $m > 18$  which suggests that  $M = 18$  is sufficient for generating the results with good accuracy in this case. However, in the next section the profile for  $\Omega_D$  is also included, which changes the coefficients  $\hat{\phi}_{n,m}$  values. Therefore, to confirm the good accuracy for all other cases we consider  $M = 50$  throughout this manuscript. Hereafter we will consider only the linear temperature profile  $T_1$  and vary other important parameters for TIM instability.

#### 4.2. Variation in precession frequency

According to equations (2) and (3), the precession frequency  $\Omega_D$  depends on both  $\psi$  and  $\kappa$ . In the previous section, we

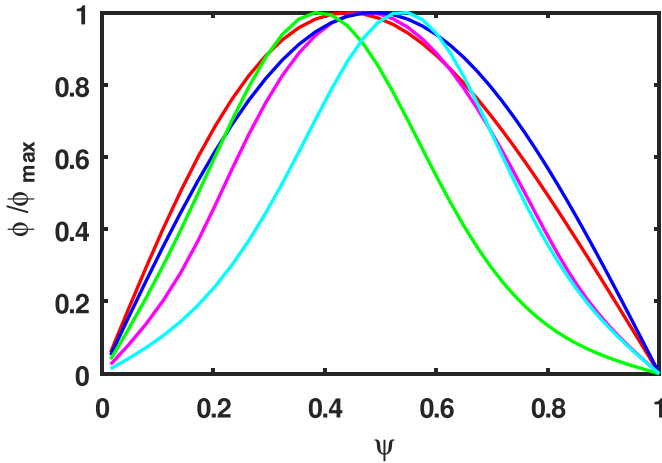


**Figure 7.** Potential solutions  $|\phi_n(\psi)|/\phi_{\max}$  for mode  $n=1$  with  $J_0$  equation (4) for the five different temperature profiles:  $T_4(\psi)$  with  $\psi_1=0.5$  (cyan line),  $T_4(\psi)$  with  $\psi_1=0.2$  (green line),  $T_1(\psi)$  (red line),  $T_2(\psi)$  (magenta line), and  $T_3(\psi)$  (blue line).

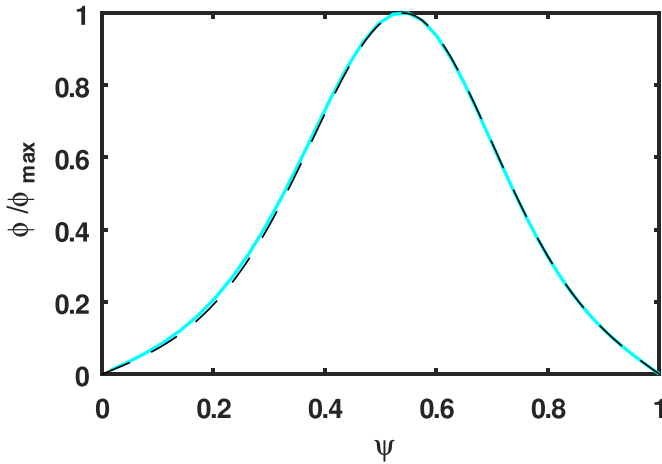


**Figure 8.** Potential solution for the temperature profile  $T_4$  with  $\psi_1=0.5$  for the highest growing mode  $n=15$ . Black dashed line presents the potential solution from the TERESA linear simulation.

consider a constant value of  $\Omega_D = 1$ . In this section we will first consider the effect of trapping parameter  $\kappa$  on the precession frequency, and second, consider the  $\psi$  dependency of  $\Omega_D$  and investigate their effects on the TIM instability in the limit of  $H_{\text{eq}} \approx E$ .

**4.2.1.  $\kappa$  dependency of  $\Omega_D$ .** In a banana orbit, the critical poloidal angle  $\theta_{\text{crit}}$ , where  $v_{\parallel} = 0$ , is linked with the trapping parameter  $\kappa$  as  $\kappa^2 = \sin^2(\frac{\theta_{\text{crit}}}{2})$ . Therefore, the acceptable values of  $\kappa$  are  $0 \leq \kappa \leq 1$ .  $\kappa=0$  is associated with the particles having almost zero parallel velocity and therefore their motions are restricted close to the center of the banana and are called deeply trapped particles.  $\kappa \sim 1$  is associated with the particles having maximum parallel velocity for the trapped particles,  $\frac{|v_{\parallel}|}{|v_{\perp}|} \sim \sqrt{\frac{B_{\max}}{B_{\min}} - 1}$ , whose reflecting point is situated near the position of the maximum magnetic field  $B_{\max}$  at the inner side of the tokamak, and are called barely trapped

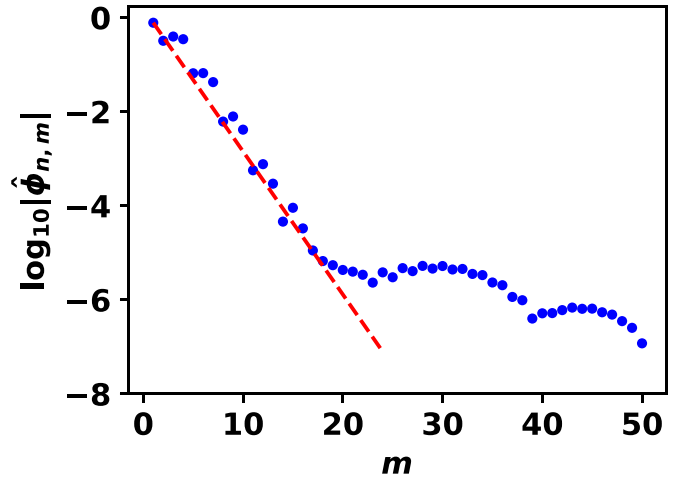


**Figure 9.** Coefficients  $\log(|\hat{\phi}_{n,m}|)$  of the function  $C_m$  versus  $m$  for  $M=50$  points along  $\psi$  in a computation for the mode  $n=15$  in the case of temperature profile  $T_4$  with  $\psi_1=0.5$ . A function  $\log[A_0 \exp(-\beta m)]$  is plotted for  $\beta=0.7$  (red dashed line).  $A_0$  is a constant.

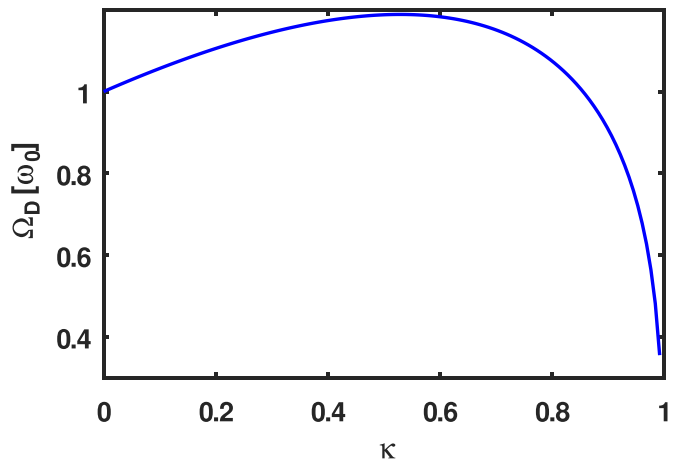


**Figure 10.** Precession frequency  $\bar{\omega}_d(\kappa)$  equation (3) for magnetic-shear  $s_0=0.8$ .

particles. Equation (3) presents the theoretical  $\kappa$  dependency of the precession frequency  $\bar{\omega}_d(\kappa)$ . Figure 10 presents this variation of  $\bar{\omega}_d$  with  $\kappa$  for a constant value of magnetic-shear  $s_0=0.8$ . In the absence of  $\psi$  dependency of precession frequency, we can write  $\Omega_D(\kappa) = \bar{\omega}_d$  from equation (2). For a realistic safety factor profile [37], the magnetic shear  $s_0(\psi)$  decreases almost linearly in  $\psi$ , and at  $\psi=0.5$  it has value  $s_0 \sim 0.8$ . In the previous section 4.1, we considered deeply trapped particles with  $\kappa=0$ . Here, we consider two different cases with the same temperature profile  $T_1$ . In one case, we consider a constant value of precession frequency  $\Omega_D = 0.6$  associated with barely trapped particles ( $\kappa \sim 1$ ), and to compare the results we reconsider the previous case with  $\Omega_D = 1$  ( $\kappa=0$ ) and temperature profile  $T_1$ . In the second case, to incorporate the effect of pitch-angle dependency in the TIM instability we consider the entire  $\Omega_D(\kappa)$  profile for the trapped particles. In this second case, the dispersion relation is calculated by doing the integration along  $\kappa$  systemically according to equation (12), which

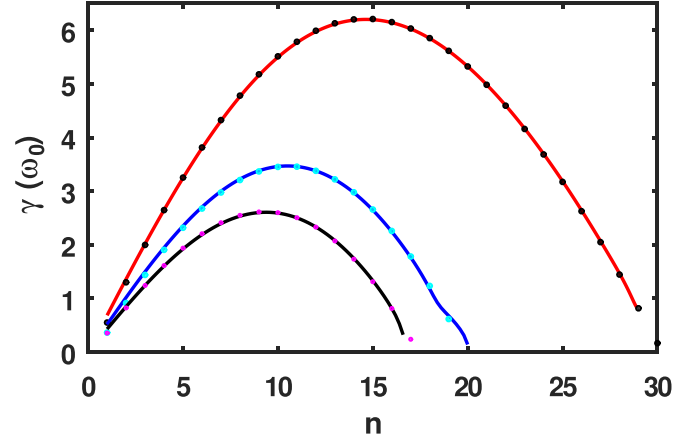
was neglected for constant  $\Omega_D$  by replacing  $\int_0^1 \kappa \mathcal{K}(\kappa^2) d\kappa = 1$ . One important aspect is that for both cases we assume that the fraction of trapped particle  $f_t \sim \sqrt{2\varepsilon}$  remains constant, which is controlled by the parameter  $C_{ad}$  in equation (12). If we consider the radial dependency of the inverse of the aspect ratio as  $\varepsilon = \frac{r}{R_0}$ , the fraction of trapped particle can be written as  $f_t \sim (1 - \psi)^{1/4}$ . This justifies our approximation  $f_t \sim \text{const.}$  throughout the region  $\psi \in [0, 1]$ . Therefore, in the first case with constant  $\Omega_D = 0.6$ , all trapped-particles are trapped near the separatrix (barely trapped), and for  $\Omega_D = 1$ , an equal amount of particles are trapped near the center of the banana. In contrast, in the second case with the entire  $\Omega_D(\kappa)$  profile, an equal amount of trapped particles are distributed over the entire trapped domain. The other essential parameters are taken from table 3.

Figure 11 presents the growth rates  $\gamma$  for different values of mode numbers  $n$  of TIM instability for these cases. Since the TIM instability occurs due to the resonance of precession frequency  $\Omega_D$  of particles with the wave frequency  $\omega$ , for low precession frequency  $\Omega_D = 0.6$  the wave with the smaller phase velocity (smaller  $\omega$ ) resonates. In the equilibrium distribution  $F_{eq}(E)$  equation (A1), there are a large number of particles near the lower velocity ( $E \equiv \frac{1}{2}mv_{G\parallel}^2 + \mu B_G$ ) compared to the higher velocity; as a consequence, the charge separation due to  $\nabla B$  drift in the presence of the temperature gradient would be higher near the lower velocity compared to the higher velocity (higher  $\Omega_D$ ), and generates a stronger electric field which helps to enhance the density perturbation of the wave. Therefore  $\Omega_D = 0.6$  has a higher growth rate compared to the case with higher precession frequency  $\Omega_D = 1$ . Since the real part of the TIM frequency  $\omega_r \propto \Omega_D$  equation (A5), for the lower  $\Omega_D = 0.6$  value  $\omega_r$  is significantly smaller compared to  $\Omega_D = 1$  case. If we consider the entire profile of  $\Omega_D(\kappa)$  for the constant magnetic-shear  $s_0 = 0.8$  (figure 10), up to  $\kappa \leq 0.85$ , the precession frequency  $\Omega_D \geq 1$ , and within  $0.85 \leq \kappa \leq 1$  it has smaller value  $\Omega_D < 1$ . Since the equilibrium distribution  $F_{eq}$  equation (A1) is independent of  $\kappa$ , there are an equal number of particles at all  $\kappa$  values. Therefore in this case, most of the particles (almost 80%) have precession frequency  $\Omega_D > 1$ ; only 20% particles have precession frequency  $\Omega_D < 1$ . As a result, the contribution from the  $\Omega_D > 1$  dominates, therefore the waves with higher phase velocity (higher  $\omega$ ) resonate with the particles, where less number of particles are available due to the Maxwellian particle distribution in  $v_{\parallel}$ . This decreases the growth rate  $\gamma$  compared to the  $\Omega_D = 1$  case. The entire  $\kappa$  dependent  $\Omega_D(\kappa)$  profile decreases the growth rate by 30%–50% compared to a constant  $\Omega_D$  value at a constant  $\kappa$  location. The dots are the growth rates for different mode numbers  $n$  from the linear TERESA simulation.

**4.2.2.  $\psi$  dependency of  $\Omega_D$ .** The theoretical dependency of the precession frequency on the radius  $r$  is given by equations (2) and (3) where both the safety factor  $q(r)$ , and magnetic shear  $s_0(r) = \frac{r}{q(r)} \frac{dq}{dr}$  depend on  $r$ . For a particular  $q(r)$  profile  $q(r) = 1.1 + 2r^2$  profile [37], the magnetic flux-function is calculated from the integration

**Table 3.** Main input parameters used for studies in section 4.2.

$\delta_{b,i}$	$\rho_{c,i}$	$C_{ad}$	$C_{pol}$	$T(\psi)$	$T_{eq}$	$n_{eq}$	$M$	$G_T$
0.1	0.03	0.1	0.1	$T_1$	1	1	50	0.25



**Figure 11.** Growth rate  $\gamma$  versus mode-number  $n$  with  $J_0$  from equation (4) and temperature  $T_1(\psi)$ , for constant values of precession frequency  $\Omega_D = 1$  (solid blue line) and 0.6 (solid red line). The black solid line is for the entire profile of  $\Omega_D(\kappa)$  equation (3). The dots are the results from the linear TERESA simulations.

$\psi(r) \sim -B_{min} \int_{r_{in}}^a \frac{r}{q(r)} dr$ , and normalized according to table 1, where  $L_{\psi} = |\psi(r_{in}) - \psi(a)|$  is the length of the simulation box in the  $\psi$  unit. Finally,  $r$  depends on  $\psi$  as,

$$r = \sqrt{\frac{q(a)}{2} \left( \frac{q(r_{in})}{q(a)} \right)^{\psi} - \frac{q(0)}{2}}, \quad (31)$$

where  $q(a)$ ,  $q(0)$  and  $q(r_{in})$  are the values of the safety factor at  $r = a$ ,  $r = 0$  and  $r = r_{in}$ , where  $a$  is the minor radius of the tokamak, and  $r_{in}$  is the lower limit of  $r$  integration in the  $\psi(r)$  expression, which helps to remove the singular nature of  $\omega_d$  in equation (2) at  $r \rightarrow 0$ . Using this expression of  $r$  equation (31) into  $q(r)$  and  $s_0(r)$ , the  $\psi$  dependent safety factor  $q(\psi)$  and magnetic shear  $s_0(\psi)$  can be obtained, and finally  $\Omega_D(\psi, \kappa)$  can be calculated from equations (2) and (3). The theoretical  $\Omega_D(\psi)$  profile for  $r_{in} = 0.2$  and  $\kappa = 0$  is presented by the solid cyan line in figure 12, which has an almost constant value  $\Omega_D \sim 1$  within  $0 \leq \psi \leq 0.75$  and after that near the core region of the tokamak ( $\psi \rightarrow 1$ ),  $\Omega_D$  increases abruptly with increase in  $\psi$ . For simplicity, first we consider how  $\Omega_D$  varies linearly with  $\psi$  as:

$$\Omega_D(\psi) = \Omega_0 + G_{\Omega} \psi, \quad (32)$$

and study the effect of  $\psi$  dependent  $\Omega_D(\psi)$  on TIM instability. Here  $\Omega_0 = 1$  is the value of  $\Omega_D$  at  $\psi = 0$ , and  $G_{\Omega}$  is the gradient in the  $\Omega_D(\psi)$  profile. This linearly increasing  $\Omega_D(\psi)$  profile for different values of  $G_{\Omega} = 0, 0.25, 0.4$  and  $0.6$  is presented in figure 12. In this section, the temperature profile  $T_1(\psi)$  with  $G_T = 0.25$ , and  $\Omega_D(\psi)$  profile with  $G_{\Omega} = 0.25$  and  $G_{\Omega} = 0$

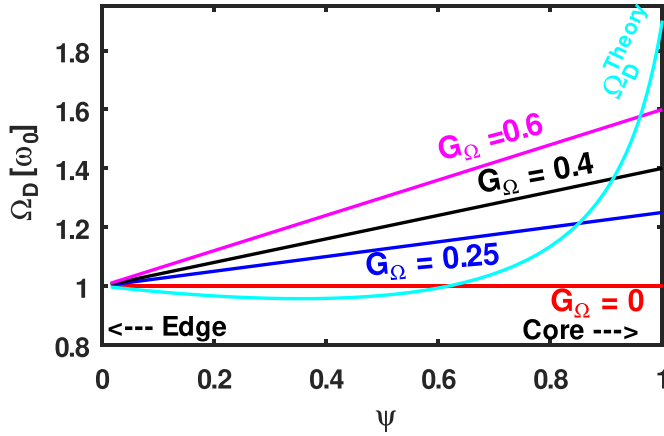


**Figure 12.** Precession frequency profiles  $\Omega_D(\psi) = \Omega_{D0} + G_\Omega \psi$ , with  $G_\Omega = 0$  (solid red line),  $G_\Omega = 0.25$  (solid blue line),  $G_\Omega = 0.4$  (solid black line) and  $G_\Omega = 0.6$  (solid magenta line).  $\Omega_{D0} = 1$  for all the cases. The theoretical  $\Omega_D(\psi)$  profile (solid cyan line) is calculated from equation (2) for  $\kappa = 0$  and  $q(r) = 1.1 + 2r^2$ .

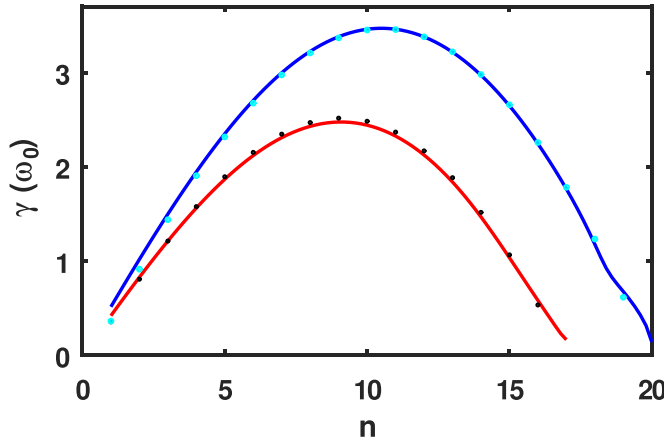


**Figure 13.** Growth rate  $\gamma$  versus mode-number  $n$  with  $J_0$  from equation (4) and temperature  $T_1(\psi)$ , and  $\psi$  dependent precession frequency  $\Omega_D(\psi) = \Omega_0 + 0.25\psi$  is presented in the solid red line. The solid blue line presents the  $\Omega_D = 1$  case. The dots are the results from the linear TERESA simulations.

equation (32) are taken into account. The other  $\Omega_D(\psi)$  profiles will be considered in the section 5. The other essential parameters are taken from table 3.

Figure 13 presents the growth rates of TIMs  $n$ , for the  $\Omega_D(\psi)$  profile equation (32) with  $G_\Omega = 0.25$ , and  $G_\Omega = 0$ . As discussed in the previous section 4.2.1, for larger  $\Omega_D$ , the number of resonant particles decreases compared to the case with a smaller  $\Omega_D$  value, and as a consequence generates a smaller growth rate of the TIM instability. Since in the  $\Omega_D$  profile with  $G_\Omega = 0.25$  equation (32), for all  $\psi$  value  $\Omega_D \geq 1$  and the temperature profile  $T_1(\psi)$  remains unchanged, the growth rate  $\gamma$  for all  $n$  values is smaller compared to the case with  $\Omega_D = 1$ . Here, the dots present the results from the linear TERESA simulation. The real part of the frequency  $\omega_r$  for the TIM instability is proportional to  $\Omega_D$  equation (A5). Therefore, in this case

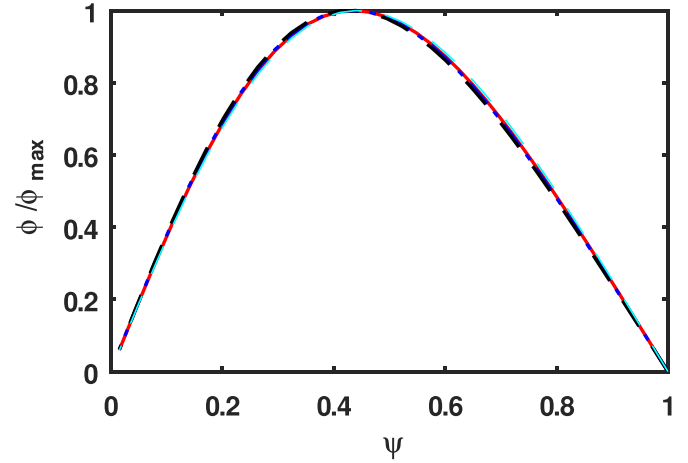


**Figure 14.** Potential solutions  $|\phi_n(\psi)|/\phi_{\max}$  for mode  $n = 1$  with  $J_0$  equation (4) for the precession frequency  $\Omega_D = 1$  (dashed cyan),  $\Omega_D = 0.6$  (solid red),  $\Omega_D = 1 + 0.25\psi$  (dashed black),  $\Omega_D(\kappa)$  (dashed blue).

$\omega_r$  will be larger compared to the case with  $\Omega_D = 1$ . However, we have not presented the  $\omega_r - n$  profile within this manuscript. Figure 14 presents the potential  $\phi_n(\psi)$  profiles for the four different  $\Omega_D$  profiles with a constant temperature profile  $T_1$ , which are almost similar. Therefore, in the limit  $H_{\text{eq}} \approx E$  the potential profiles are almost independent of the precession frequency profiles. One important point is that in case of  $\psi$  dependent precession frequency  $\Omega_D(\psi)$ , the equilibrium Hamiltonian  $H_{\text{eq}}$  depends on  $\psi$  in a more complicated manner, which was linear in  $\psi$  for a constant  $\Omega_D$ . Therefore, the limit  $H_{\text{eq}} \approx E$  is no longer a good approximation; one has to consider the expression of the exact Hamiltonian. We will discuss this issue in the next section.

## 5. Effect of inverse gradient length of equilibrium Hamiltonian $\kappa_\Lambda$ on TIM instability

In this section, we consider the dispersion relation (equations (13)–(15)), which is derived from the exact Hamiltonian expression equation (7) in section 2. In this case, according to equation (20), the threshold value of  $\kappa_T$  for TIM instability is higher compared to the case in the limit  $H_{\text{eq}} \approx E$ . Therefore, in this section we have considered the temperature profile  $T_1(\psi)$  with gradient  $G_T = 3$  and 2 in equation (30) which was 0.25 in the previous cases section 4 in the limit  $H_{\text{eq}} \approx E$ . To investigate the effect of  $\kappa_\Lambda$  on TIM instability, we consider precession frequency  $\Omega_D(\psi)$  according to the theoretical expression equations (2) and (3) and also the simplified expression in the form of equation (32) with three different values of gradient  $G_\Omega = 0, 0.4$  and  $0.6$ . Figure 12 presents all these  $\Omega_D(\psi)$  profiles. Considering the theoretical expression of  $\Omega_D(r, \kappa)$  equations (2) and (3) and the safety factor profile as  $q(r) = 1.1 + 2r^2$ , the expression of  $\Lambda_D(r, \kappa)$  can be written as,

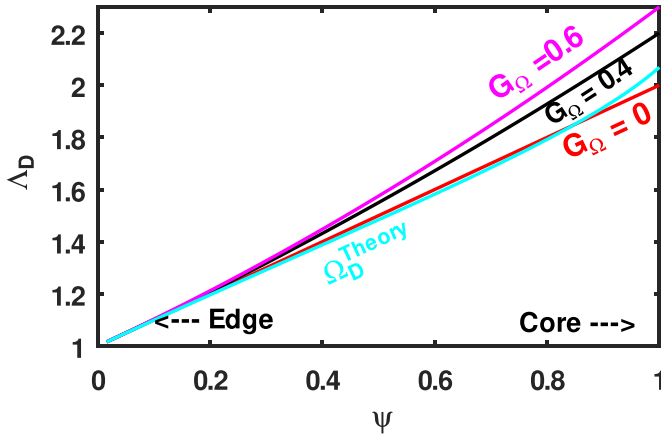


**Figure 15.** Different profiles of  $\Lambda_D(\psi) = 1 + \int \Omega_D(\psi) d\psi$ , associated with three different  $\Omega_D(\psi)$  profiles. Solid red, black and magenta lines are associated with  $G_\Omega = 0, 0.4$  and  $0.6$ , respectively in equation (32). The solid cyan line presents the  $\Lambda_D(\psi)$  profile for the theoretical expression of  $\Omega_D(\psi)$  equations (2) and (3).

**Table 4.** Main input parameters used for studies in section 5.

$\delta_{b,i}$	$\rho_{c,i}$	$C_{ad}$	$C_{pol}$	$T(\psi)$	$T_{eq}$	$n_{eq}$	$M$	$G_T$
0.1	0.03	0.1	0.1	$T_1$	1	1	50	3, 2

$$\Lambda_D(r, \kappa) = 1 + \frac{4}{q(a) \ln \left( \frac{q(a)}{q(r_{in})} \right)} \left[ -\lambda_2(\kappa)r + 4\sqrt{2q(0)} \right. \\ \times \lambda_1(\kappa) \tan^{-1} \left( \sqrt{\frac{2}{q(0)}} r \right) + \lambda_2(\kappa) \sqrt{\frac{1}{2} (q(a) - q(0))} \\ \left. - 4\sqrt{2q(0)} \lambda_1(\kappa) \tan^{-1} \left( \sqrt{\frac{q(a)}{q(0)}} - 1 \right) \right], \quad (33)$$

where  $\lambda_1(\kappa) = \left( \frac{\mathcal{E}(\kappa^2)}{\mathcal{K}(\kappa^2)} + \kappa^2 - 1 \right)$ , and  $\lambda_2(\kappa) = \left( 10 \frac{\mathcal{E}(\kappa^2)}{\mathcal{K}(\kappa^2)} + 8\kappa^2 - 9 \right)$ . Substituting the value of  $r$  from equation (31),  $\psi$  dependent  $\Lambda_D(\psi, \kappa)$  can be calculated. This  $\Lambda_D(\psi)$  profile equation (33) with  $\kappa = 0$  is presented in figure 15 with a solid cyan line. The other profiles of  $\Lambda_D(\psi)$  in figure 15 are, for the simplified  $\Omega_D(\psi)$  profile in equation (32) with  $G_\Omega = 0, 0.4$  and  $0.6$ . Therefore, the  $\Lambda_D(\psi)$  profile for the simplified  $\Omega_D(\psi)$  expression equation (32) with  $G_\Omega = 0$ , is almost similar with the  $\Lambda_D(\psi)$  profile for the theoretical expression of  $\Omega_D(\psi, \kappa)$  with  $\kappa = 0$ . The values of  $\kappa_\Lambda = \frac{\Omega_D}{\Lambda_D}$  for all the four profiles at  $\psi = 0$  is  $\kappa_\Lambda = 1$ , and then decreases with different rates as  $\psi$  increases. Here we first consider the temperature profile  $T_1$  with gradient  $G_T = 3$  and study the TIM instability for all the four  $\Lambda_D$  and  $\Omega_D$  profiles. Then, in order to understand the effect of temperature gradient on TIM instability in this new modified model with an exact equilibrium Hamiltonian, we decrease the temperature gradient  $G_T = 2$  and consider the theoretical expression of  $\Omega_D$  as equations (2) and (3) and the  $\Lambda_D$  profile as equation (33) for  $\kappa = 0$ . Other essential parameters are taken from table 4. The potential solution  $\phi_n(\psi)$  is obtained by solving the differential equation (16) with the

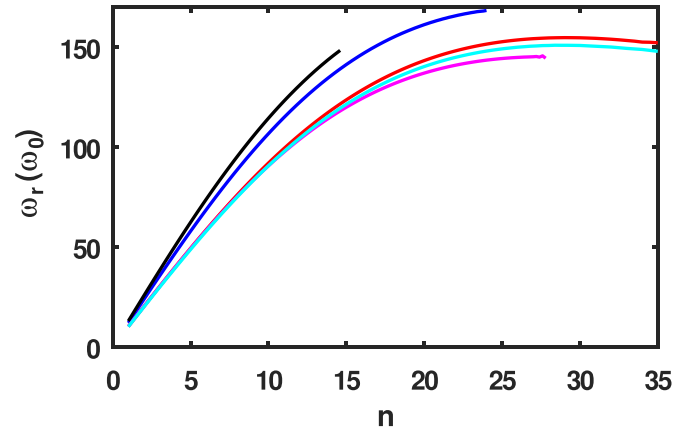


**Figure 16.** Real part of the frequency  $\omega_r$  of TIM instability for  $T_1$  with  $G_T = 3$  and  $\Omega_D(\psi)$  profiles according to the theoretical expression equations (2) and (3) with  $\kappa = 0$  (solid cyan line), and from the simplified expression equation (32) with  $G_\Omega = 0$  (solid red line),  $G_\Omega = 0.4$  (solid blue line) and  $G_\Omega = 0.6$  (solid black line). The solid magenta line denotes  $G_T = 2$  and the theoretical expression of  $\Omega_D(\psi)$ .

expression for the  $\mathcal{N}_n$  equation (13), using the spectral method. Due to the high temperature gradient  $G_T = 3$  and 2, the value of  $T(\psi)$  is very high compared to previous cases, which makes the particle equilibrium distribution  $F_{eq}(\psi, \kappa, E)$  equation (10) broaden to a high  $E$  value. Therefore, in this case we have to increase the maximum limit of  $E$  as  $E \in [0, 45]$  for the numerical integration along the  $E$  direction, whereas for the previous cases with  $G_T = 0.25$  we considered  $E \in [0, 20]$ .

Figure 16 presents the real part of the TIM instability for different mode numbers  $n$  for all these five cases. According to equation (18), the case with the higher  $\kappa_\Lambda$  value has higher  $\omega_r$ , therefore the case with the larger  $G_\Omega$  has higher  $\omega_r$ . In the theoretical expression of  $\Omega_D$  for  $\kappa = 0$  the value of  $\Omega_D \sim 1$  for  $\psi \in [0, 0.75]$  and only for  $\psi \geq 0.75$ , it has values greater than the unity. Therefore, the  $\omega_r$  profile of TIM instability, in this case is very close to the case with the  $\Omega_D = 1$  profile. Keeping the  $\Omega_D$  profile fixed, if we decrease the  $\kappa_T$  value by decreasing  $G_T = 2$ , the  $\omega_r$  value decreases by a very small amount. Figure 17 presents the growth rate  $\gamma$  for different mode numbers  $n$  of TIM instability. Since  $\kappa_\Lambda$  in the expression of  $\mathcal{N}$  equation (13) reduces the effect of  $\kappa_T$ , the growth rates in all these cases are very small compared to the previous cases with  $\kappa_\Lambda = 0$  and  $\Lambda = 1$ . Moreover, the increase in  $\kappa_\Lambda$  decreases the  $\gamma$  value. Among the three  $\Omega_D$  profiles, the cases with highest  $G_\Omega = 0.6$  value have a higher  $\kappa_\Lambda$  value, which gives the lowest growth rate. As in the theoretical expression of  $\Omega_D$  for  $\kappa = 0$  has value  $\Omega_D \sim 1$  within the region  $\psi \in [0, 0.75]$  and after that it increases, therefore the growth rate  $\gamma$  in this case is almost similar to the case with  $\Omega_D = 1$  and has a slightly smaller value due to  $\Omega_D \geq 1$  within the region  $\psi \geq 0.75$ . Therefore, we can conclude that the complicated theoretical expression of  $\Omega_D$  for  $\kappa = 0$  can be simplified as  $\Omega_D = 1$  with a good accuracy for studying the TIM instability. If we decrease the temperature gradient  $G_T = 2$ , for the same theoretical  $\Omega_D$  profile, the growth rate  $\gamma$  decreases by a significant amount ( $\sim 70\%$ ) due to

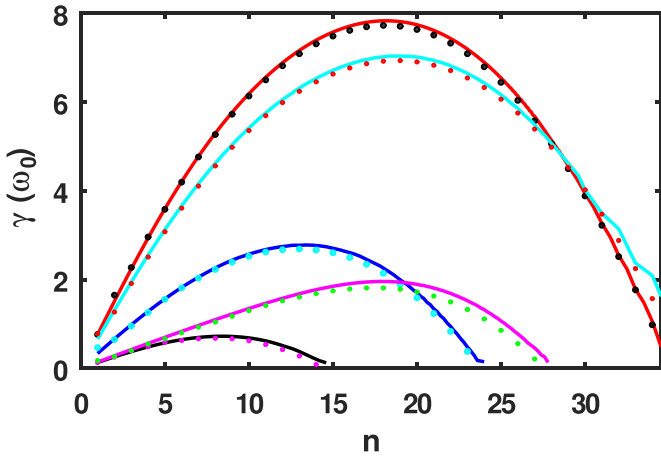


**Figure 17.** Growth rate  $\gamma$  of different modes  $n$ ,  $T_1$  with  $G_T = 3$  and different  $\Omega_D(\psi)$  profiles, solid red, blue and black lines are for simplified  $\Omega_D(\psi)$  expression equation (32) with  $G_\Omega = 0$ ,  $G_\Omega = 0.4$  and  $G_\Omega = 0.6$  respectively. Solid cyan line:  $\Omega_D(\psi)$  theoretical expression equations (2) and (3) with  $\kappa = 0$ ,  $G_T = 3$ . Solid magenta line: for  $G_T = 2$  and the theoretical expression of  $\Omega_D(\psi)$ . The dots are the results from linear TERESA simulations.

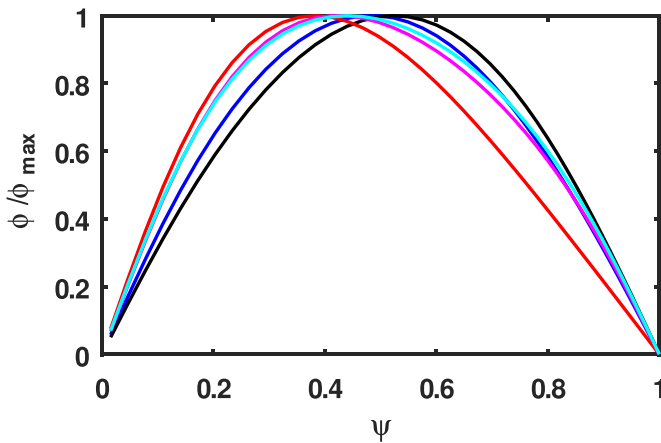


**Figure 18.** Potential solutions  $|\phi_n(\psi)|/\phi_{\max}$  for mode  $n = 1$ ,  $T_1$  with  $G_T = 3$  and different  $\Omega_D(\psi)$  profiles. Solid red, blue and black lines are for simplified  $\Omega_D(\psi)$  expression equation (32) with  $G_\Omega = 0$ ,  $G_\Omega = 0.4$  and  $G_\Omega = 0.6$  respectively. Solid cyan line:  $\Omega_D(\psi)$  theoretical expression equations (2) and (3) with  $\kappa = 0$ . Solid magenta line: for  $G_T = 2$  and the theoretical expression of  $\Omega_D(\psi)$ .

the decrease in the  $\kappa_T$  value. The dots are the results from the linear TERESA simulations for all cases. Figure 18 presents the potential profiles  $\phi_n(\psi)$  for  $n = 1$  and for all the five different cases with different  $\Omega_D(\psi)$  profiles. The  $\phi_n(\psi)$  solution is different for different  $\Omega_D(\psi)$  profiles, whereas the  $\phi_n(\psi)$  profiles for different  $\Omega_D$  profiles are almost similar for the limit  $H_{\text{eq}} \approx E$ . In this new model  $\phi_n(\psi)$  profiles are varying with both the temperature profiles and the precession frequency profiles.

Throughout this paper, in the linear analysis, the nonlinear term  $[J_{0,s}\phi_s\tilde{f}_s]_{\alpha,\psi}$  is neglected, by considering that  $\tilde{f}_s$  is very small and the equilibrium distribution function  $F_{\text{eq},s}$  remains unchanged during the time evolution. However, we have verified that these assumptions are valid only for small amplitude

potential  $|e\phi/T| \ll 1$ , and as the amplitude of the potential grows beyond a certain value ( $e\phi/T \sim 0.1$ ), due to strong nonlinear wave-particle and/or wave-wave interactions, the growth rate  $\gamma(t)$  decreases and finally nonlinear saturation occurs. Since the nonlinear evolution of the TIM is not the focus of this study, we have not presented those results here.

## 6. Conclusions

In this work, we proposed an alternative way to solve a reduced gyro-bounce averaged kinetic model for trapped particle dynamics within a linear limit using a spectral method [28, 29]. This method is computationally very fast compared to the semi-Lagrangian method based solver TERESA [8, 25, 26]. Using this method we have investigated the TIM instability. Unlike the local linear analysis [9] of trapped particle mode instability, our proposed method can incorporate the entire profiles ( $0 \leq \psi \leq 1$ ) of all the essential parameters, and is not restricted by their local values at  $\psi = 0$ . In this respect, our method is a *global-linear analysis* of trapped particle modes instability. Also the dependency of trapped particle drift velocity on magnetic poloidal flux function  $\psi$ , is newly incorporated in the gyro-bounce averaged trapped particle model by considering the exact expression of equilibrium Hamiltonian  $H_{\text{eq}}(\psi, \kappa) = E\Lambda_D(\psi, \kappa)$  in quasi-neutrality equation and gyro-bounce averaged equilibrium distribution function  $F_{\text{eq}}$ , which were previously simplified in the limit  $H_{\text{eq}} \approx E$ . With this new Hamiltonian, a new quantity  $\kappa_\Lambda$ , that measures the inverse gradient length of the equilibrium Hamiltonian, appears in the dispersion relation of the TIM instability. All the previous results in the limit  $H_{\text{eq}} \approx E$  can be recovered by substituting  $\Lambda_D = 1$  and  $\kappa_\Lambda = 0$ . The quantity  $\kappa_\Lambda$  reduces the effect of  $\kappa_T$  and  $\kappa_n$ , and as a consequence reduces the growth rate of TIM instability.

In tokamak plasma, trapped particle modes (resonant-branch) are driven by the resonant interaction with the precession motion of trapped particles, and these modes become unstable in the presence of density inhomogeneity, a gradient in the magnetic field, and above a critical gradient of temperature. Therefore, the effect of different temperature profiles  $T(\psi)$  and precession-frequency  $\Omega_D$  on the linear TIM instability are investigated. The results for all the cases are compared with the linear TERESA simulations. First we consider the model in the limit  $H_{\text{eq}} \approx E$  and validate our spectral method based solver with the TERESA simulation for the expression of gyro-bounce average operator  $J_0 = 1$ . The solutions from this  $J_0 = 1$  case are used during the calculation of gyro-bounce average of potential  $J_0\phi$  using the Padé expression, for the mode number  $n = 1$  at the first iteration. To study the effect of temperature gradient on TIM instability, we vary the temperature profiles which are relevant to different regions of a tokamak plasma experiment and keep fixed the normalized precession frequency value  $\Omega_D = 1$ . Depending on the inverse temperature gradient length  $\kappa_T$  value, the growth rate of TIM instability for different temperature profiles is different. The profile with a higher  $\kappa_T$  value gives a higher growth rate, and the highest growing mode also shifted toward a higher mode

number. The real part of frequency  $\omega_r - n$  profile for all the temperature profiles with a constant  $\Omega_D$  value, follow a relation  $\omega_r \sim 2n\Omega_D$ . We have then studied the effect of variations in precession frequency profile  $\Omega_D$  on TIM instability in the limit  $H_{\text{eq}} \approx E$ . For lower values of  $\Omega_D$ , the waves with smaller velocity make resonance with the trapped ion motion. Due to Maxwellian energy distribution of particles, a large number of particles near the lower velocity take part in the instability generation mechanism, and yield stronger instability for smaller  $\Omega_D$ . Hence, we get larger growth rates for smaller  $\Omega_D$ . The effect of pitch-angle dependency of trapped particles on the TIM instability is investigated by considering the entire  $\kappa$  dependent profile of  $\Omega_D$ . Since for a constant magnetic shear  $s_0 = 0.8$ , for most of the  $\kappa$  value  $\Omega_D(\kappa) > 1$  except near the separatrix  $0.85 \leq \kappa \leq 1$ , the growth rate of TIM instability is smaller compared to the  $\Omega_D = 1$  case. The  $\psi$  dependency of the precession frequency  $\Omega_D(\psi)$  on TIM instability in the limit  $H_{\text{eq}} \approx E$ , is also investigated for a simplified linearly increasing  $\Omega_D$  profile. Since for this profile, the values of precession frequency  $\Omega_D > 1$  for all the  $\psi > 0$  locations, the growth rate of the TIM instability is smaller than the case with  $\Omega_D = 1$ . In the limit  $H_{\text{eq}} \approx E$ , the potential profiles are almost independent of different  $\Omega_D(\psi, \kappa)$  profiles.

The effect of  $\psi$  dependency of  $\Omega_D$  on the TIM instability in the newly modified model with exact equilibrium Hamiltonian expression is investigated by considering a theoretical expression of  $\Omega_D$  and a simplified linearly increasing function of  $\Omega_D$ . For  $\kappa = 0$  the theoretical expression of  $\Omega_D$  has value  $\Omega_D \sim 1$  within the region  $0 \leq \psi \leq 0.75$ , and after that it increases. The growth rate  $\gamma$  of TIM instability for the particular theoretical  $\Omega_D$  profile is almost similar to the  $\Omega_D = 1$  case, and due to  $\Omega_D \geq 1$  with in the region  $0.75 \leq \psi \leq 1$ , it is slightly smaller than  $\Omega_D = 1$  case. With the increase of the slope  $G_\Omega$  in the simplified linearly increasing  $\Omega_D$  profile, which increases  $\kappa_\Lambda$  value, the growth rate of different modes  $n$  for the instability decreases. Moreover, after the new modification, the decrease in slope  $G_T$  of the temperature profile (decrease  $\kappa_T$  value) for a fixed  $\Omega_D$  profile, decreases the growth rate, which is consistent with the results in the limit  $H_{\text{eq}} \approx E$ . In this newly modified model the potential solutions are different for different  $\Omega_D$  profiles.

## Data availability statement

All data that support the findings of this study are included within the article (and any supplementary files).

## Acknowledgments

This work was funded by the Agence Nationale de la Recherche for the Project GRANUL (ANR-19-CE30-0005). This work was granted access to the HPC resources of EXPLOR (Project No. 2017M4XXX0251), and of CINECA MARCONI under Project FUA35 GSNTITE. This work has been carried out within the framework of the EUROfusion Consortium, funded by the European Union via the Euratom Research

and Training Programme (Grant Agreement No. 101052200-EUROfusion). Views and opinions expressed are however those of the author(s) only and do not necessarily reflect those of the European Union or the European Commission. Neither the European Union nor the European Commission can be held responsible for them. We are grateful to the anonymous reviewers for their constructive remarks.

## Appendix. Linear analysis within the limit $H_{\text{eq}} \approx E$

The global linear analysis for the case with the limit  $H_{\text{eq}} \approx E$  can be derived in a similar way, as discussed in section 2.1. Here the normalized equilibrium distribution  $F_{\text{eq},s}$  is independent of  $(\alpha, \kappa, t)$ , and has the form of a two-dimensional (2D) Maxwellian energy distribution function

$$F_{\text{eq},s}(\psi, E) = \frac{n_s(\psi)}{T_s^{3/2}(\psi)} \exp\left(-\frac{E}{T_s(\psi)}\right). \quad (\text{A1})$$

After substituting  $F_{\text{eq},s}$  from equation (A1),  $\tilde{f}_s = \sum_{n,\omega} f_{s,n,\omega}(\psi, E, \kappa) \exp\{i(n\alpha - \omega t)\}$  and  $\tilde{\phi} = \sum_{n,\omega} \phi_{n,\omega}(\psi) \exp\{i(n\alpha - \omega t)\}$ , in equation (9), the solution of the Vlasov equation in Fourier space becomes,

$$f_{s,n,\omega}(\psi, E, \kappa) = \frac{n \left[ \kappa_n(\psi) + \kappa_T(\psi) \left( \frac{E}{T_s(\psi)} - \frac{3}{2} \right) \right]}{Z_s^{-1} n \Omega_D(\kappa) E - \omega} \times \{J_{0,n,s} \phi_{n,\omega}(\psi)\} F_{\text{eq},s}(\psi, E). \quad (\text{A2})$$

In this case the elementary volume in phase-space can be written as  $d^3v = 4\pi\sqrt{2}m^{-3/2}\sqrt{E}dE\frac{d\lambda}{4\Omega_D}$ . Using this volume element  $d^3v$  and  $f_{n,\omega}$  from equation (A2) the expression of  $\mathcal{N}_s$  in equation (12) can be written (in the limit of a constant pitch-angle) as,

$$\mathcal{N}_{n,s}(\psi) = \frac{1}{n_{\text{eq}}} \int_0^\infty J_{0,n,s} \left[ \frac{\kappa_n(\psi) + \kappa_T(\psi) \left( \frac{E}{T_s(\psi)} - \frac{3}{2} \right)}{Z_s^{-1} \Omega_D(E - \chi_s)} \right] \times \{J_{0,n,s} \phi_{n,\omega}(\psi)\} \frac{n_s(\psi)}{T_s^{3/2}(\psi)} \exp\left(-\frac{E}{T_s(\psi)}\right) \sqrt{E} dE, \quad (\text{A3})$$

where  $\chi_s = \frac{\omega}{nZ_s^{-1}\Omega_D}$ . The expression of  $C_n$  equation (14) remains unaltered. Therefore the dispersion relation becomes,

$$C_n \phi_{n,\omega} = \mathcal{N}_{n,i}^* \phi_{n,\omega} - \mathcal{N}_{n,e}^* \phi_{n,\omega} \quad (\text{A4})$$

where  $\mathcal{N}_{n,s}^* = \frac{\mathcal{N}_{n,s}}{\phi_{n,\omega}}$ . The final form of the second-order differential equation for  $\phi_n(\psi)$  equation (16) remains unchanged, except  $\mathcal{N}_n^*$  inside  $Q_n(\psi)$  equation (17), where  $\mathcal{N}$  is given by equation (A3). Comparing the expressions of  $\mathcal{N}$  from equations (13) and (A3), the main difference in the dispersion relation arises due to the absence of the term  $-\frac{E\Lambda_D}{T} \kappa_\Lambda$  in  $\mathcal{N}$  in the limit  $H_{\text{eq}} \approx E$ , which reduces the effective contribution from  $\kappa_n$  and  $\kappa_T$  in the case of an exact Hamiltonian. Therefore the growth rate of the TIM instability in the limit

$H_{\text{eq}} \approx E$ , is significantly higher compared to the case with the exact Hamiltonian.

As discussed in section 2.2 the local linear stability analysis of this reduced gyro-bounce averaged model in the limit  $H_{\text{eq}} \approx E$  can be performed and the threshold frequency value of TIM instability can be derived as [9]:

$$\omega_r = \frac{\left(\frac{3}{2}\kappa_T - \kappa_n\right)}{\kappa_T} n\Omega_D T_0, \quad (\text{A5})$$

where  $T_0$  is the temperature at  $\psi = 0$ . The threshold value of  $\kappa_T$  for the TIM instability can be written as

$$\kappa_{T,\text{th}} = \frac{C_n \Omega_{D0}}{\int_0^\infty J_{0,n}^2 \exp(-\xi) \sqrt{\xi} d\xi} \quad (\text{A6})$$

where  $\xi = \frac{E}{T}$ .

## ORCID iDs

D Mandal  <https://orcid.org/0000-0001-8871-4785>

M Lesur  <https://orcid.org/0000-0001-9747-5616>

E Gravier  <https://orcid.org/0000-0002-8911-5546>

J N Sama  <https://orcid.org/0000-0002-0832-4312>

A Guillevic  <https://orcid.org/0000-0003-0182-3677>

Y Sarazin  <https://orcid.org/0000-0003-2479-563X>

X Garbet  <https://orcid.org/0000-0001-5730-1259>

## References

- [1] Dimits A M, Cohen B I, Nevins W M and Shumaker D E 2001 *Nucl. Fusion* **41** 1725
- [2] Guzdar P N, Chen L, Tang W M and Rutherford P H 1983 *Phys. Fluids* **26** 673
- [3] Ottaviani M, Horton W and Erba M 1997 *Plasma Phys. Control. Fusion* **39** 1461
- [4] Stallard B W et al 1999 *Phys. Plasmas* **6** 1978
- [5] Dannert T and Jenko F 2005 *Phys. Plasmas* **12** 072309
- [6] Brower D L, Peebles W A, Kim S K, Luhmann N C, Tang W M and Phillips P E 1987 *Phys. Rev. Lett.* **59** 48
- [7] Eubank H et al 1979 *Phys. Rev. Lett.* **43** 270
- [8] Depret G, Garbet X, Bertrand P and Ghizzo A 2000 *Plasma Phys. Control. Fusion* **42** 949
- [9] Drouot T, Gravier E, Reveille T, Ghizzo A, Bertrand P, Garbet X, Sarazin Y and Cartier-Michaud T 2014 *Eur. Phys. J. D* **68** 280
- [10] Garbet X 2001 *Plasma Phys. Control. Fusion* **43** A251
- [11] Ghizzo A and Palermo F 2015 *Phys. Plasmas* **22** 082304
- [12] Chen H and Chen L 2022 *Phys. Rev. Lett.* **128** 025003
- [13] Drouot T et al 2015 *Phys. Plasmas* **22** 082302
- [14] Waltz R E, Kerbel G D and Milovich J 1994 *Phys. Plasmas* **1** 7
- [15] Ottaviani M, Romanelli F, Benzi R, Briscolini M, Santangelo P and Succi S 1990 *Phys. Fluids B* **2** 1
- [16] Dorland W and Hammett G W 1993 *Phys. Fluids* **5** 812
- [17] Lin Z and Chen L 2001 *Phys. Plasmas* **8** 1447
- [18] Sydora R D, Decyk V K and Dawson J M 1996 *Plasma Phys. Control. Fusion* **38** A281
- [19] Lee W W 1987 *J. Comput. Phys.* **72** 243
- [20] Idomura Y, Tokuda S and Kishimoto Y 2003 *Nucl. Fusion* **43** 234
- [21] Manfredi G, Shoucri M, Dendy R O, Ghizzo A and Bertrand P 1996 *Phys. Plasmas* **3** 202
- [22] Kwon J-M, Qi L, Yi S and Hahmba T S 2017 *Comput. Phys. Commun.* **215** 81
- [23] Fong B H and Hahm T S 1999 *Phys. Plasmas* **6** 188
- [24] Ghizzo A, Mouden M E, Sarto D D, Garbet X and Sarazin Y 2011 *Transp. Theory Stat. Phys.* **40** 382
- [25] Sarazin Y, Grandgirard V, Fleurence E, Garbet X, Ghendrih P, Bertrand P and Depret G 2005 *Plasma Phys. Control. Fusion* **47** 1817
- [26] Darinet G, Ghendrih P, Sarazin Y, Garbet X and Grandgirard V 2008 *Commun. Nonlinear Sci. Numer. Simul.* **13** 53
- [27] Lesur M et al 2020 *Nucl. Fusion* **60** 036016
- [28] Gravier E, Plaut E, Caron X and Jenny M 2013 *Eur. Phys. J. D* **67** 7
- [29] Gravier E and Plaut E 2013 *Phys. Plasmas* **20** 042105
- [30] Drouot T 2015 *PhD Thesis* Université de Lorraine
- [31] Plemelj J 1908 *Mon. hefte Math. Phys.* **19** 205
- [32] Priymak V G and Miyazaki T 1998 *J. Comput. Phys.* **142** 370
- [33] Lagarias J C, Reeds J A, Wright M H and Wright P E 1998 *SIAM J. Opt.* **9** 112
- [34] Lesur M, Cartier-Michaud T, Drouot T, Diamond P H, Kosuga Y, Réveillé T, Gravier E, Garbet X, Itoh S-I and Itoh K 2017 *Phys. Plasmas* **24** 012511
- [35] Jacquinet J and (the JET Team) 1999 *Plasma Phys. Control. Fusion* **41** A13
- [36] Pánek R, Adámek J, Aftanas M, Bilková P and et al 2015 *Plasma Phys. Control. Fusion* **58** 014015
- [37] Gobbin M et al 2011 *Phys. Plasmas* **18** 062505